Master Thesis, Department of Geosciences

Characterizing seismic interference from marine seismic multi-component data

Elyas Hassanzadeh Haghighi

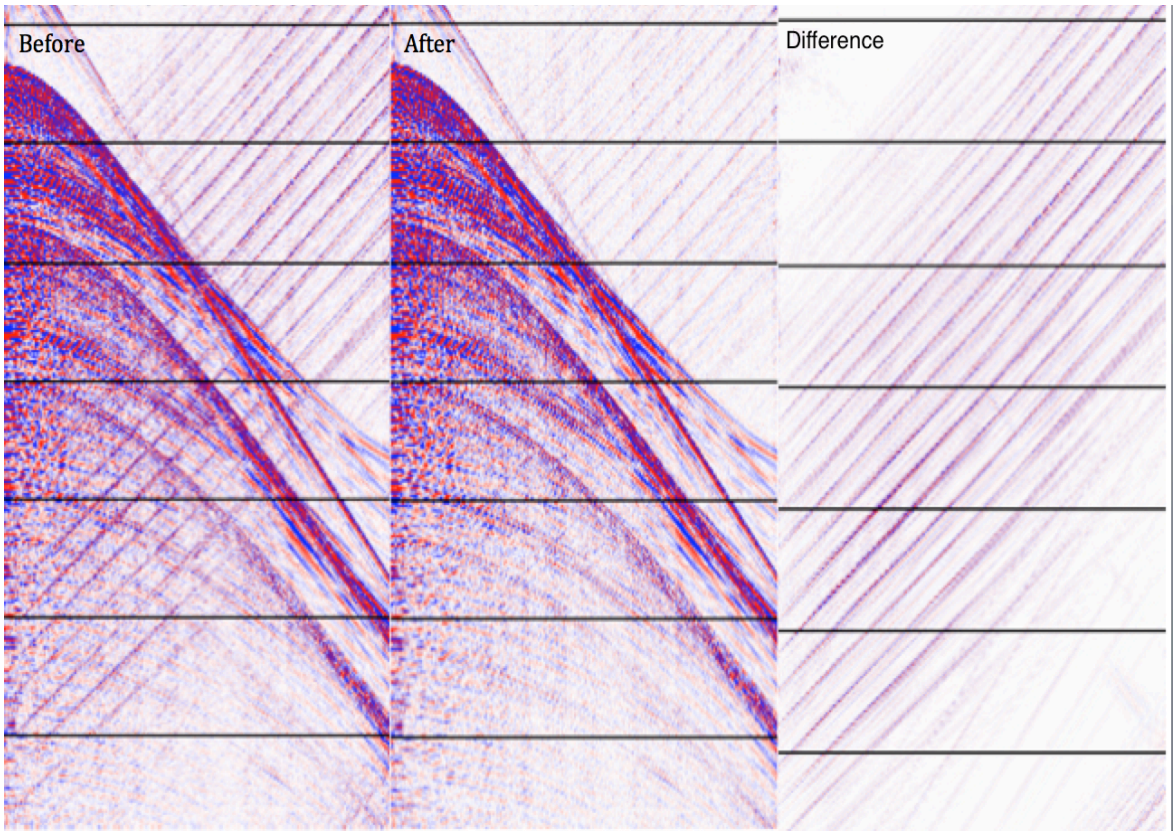

UNIVERSITY OF OSLO
FACULTY OF MATHEMATICS AND NATURAL SCIENCES

Characterizing seismic interference from seismic multi-component data

Elyas Hassanzadeh Haghighi

Master Thesis in Geosciences

Discipline: Geology

Department of Geosciences

Faculty of Mathematics and Natural Sciences

University of Oslo

June, 2014

ACKNOWLEDGMENT

This thesis work has been done in collaboration between the University of Oslo and CGG. The main part of the work has been carried out during my work in CGG at Skøyen and Lysaker offices. I am thankful to many CGG personnel at both Skøyen and Lysaker bases for making a friendly atmosphere and their assistance in various ways during my research work. I am truly indebted to my external supervisors Dr. Thomas Elboth and Dr. Charlotte Sanchis in CGG. Discussions and suggestions from Dr. Thomas Elboth have inspired many ideas during the development of this thesis.

It would have been impossible to write this thesis without my internal supervisor, Prof. Leiv J. Gelius, whose continuous help, encouragement and supervision, has enabled me to acquire and develop new analytical techniques.

My thanks are extended to friends, family and colleagues for their support and good company during my one year long thesis work.

Elyas H. Haghighi

May 31, 2013

ABSTRACT

This master thesis in Geophysics is about detecting and attenuating seismic interference noise. The thesis is written in collaboration with the Marine R&D Department at CGG and Department of Geosciences at the University of Oslo.
The main focus of this work was to detect and attenuate seismic interference from 2D marine seismic data measured by three-component (3C) streamers. The multicomponent measurement consist of pressure (P) and particle velocity component V_y and V_z.

During the course of the project it was found that the two velocity sensor components V_y and V_z could not be used to characterize and detect the seismic interference (SI). The reason is that they are very sensitive to streamer born noise such as transversal vibration noise. Such noise will be almost perpendicular to the direction of the propagating wave in the water column. Thus the particles do not move along with the wave, but oscillate up and down around their equilibrium position as the wave pass by.

Therefore, in this thesis we had to limit the analyses to pressure data only. Unlike velocity sensors, hydrophones can be made insensitive to vibration by design. Therefore, the development of multicomponent streamers that measure particle velocity is more challenging than design of conventional streamers that measure pressure only. The attenuation of seismic interference in this work was carried out using a τ-p to common-p method which after such transformation and sorting, makes the SI appear with a random character which can be efficiently removed.

In the analysis, data before and after removal of SI were compared at three different processing steps: pre-stack in the form of source gather, stacked section and post-stack migrated sections. At the level of stacking, the SI corrected dataset performed slightly better. However, after migration, both datasets performed equally well. This result is not surprising, since the data considered here were dominated by SI with a moveout opposite that of the recorded data. In cases where the two moveouts are fairly similar, the attenuation of SI is believed to play a more important role.

TABLE OF CONTENTS

LIST OF FIGURES

1. INTRODUCTION

The objective of this master thesis in Geophysics has been to identify and remove seismic interference (SI) noise. This thesis is written in collaboration with the Marine R&D Department at CGG and Department of Geosciences at the University of Oslo.
The data considered has been acquired employing multi-component streamers. Most of the development and testing have been carried out in MATLAB. However, the final results and comparisons have been done using CGG processing software Uniseis.

1.1 Motivation and aim of thesis

Seismic interference (SI) noise experienced during marine acquisitions is a common problem in the seismic industry since it reduces the quality of the seismic data.

One aim of this thesis is to identify SI among all incoming noise and then attenuate it. Originally, the idea was to remove SI from marine seismic data measured by streamers that record two particle velocity components (V_y and V_z) in addition to the pressure (P) field. During the course of the work it was found that only P-waves could be used due to too much vibrational noise polluting the velocity sensors.

1.2 Outline of the thesis

This thesis consists of nine chapters. The first chapter gives the motivation and outline of the thesis. The second chapter describes different types of noise recorded during the seismic survey. The third chapter discusses the main characteristics of SI followed by a discussion of common methods to remove it as presented in chapter four. One of the methods referred to is the "τ-p to common-p" technique, which is the one used in this thesis.

Chapter five discusses processing strategies for the attenuation of seismic interference. In chapter six the geology of the acquisition area is briefly discussed and the acquisition parameters being introduced. Results from the actual data processing are given in chapter seven followed by a discussion in chapter eight. This discussion forms the basis of the final conclusions introduced in chapter nine. The problem of identifying the dip of SI has been

programmed in MATLAB. Most of the other results have been produced and visualized in the CGG processing package Uniseis.

2. WHAT IS SEISMIC NOISE?

Seismic data can in general be regarded as a combination of signal and noise. Seismic noise is therefore unwanted energy that often appears in marine seismic recordings. It degrades data quality and can often be difficult to attenuate. The causes and effects can vary from survey to survey. Several types of noise can be expected and different methods exist to remove those.

In Schlumbergers oilfield glossary, noise is defined as (Schlumberger, 2013):

"Anything other than desired signal. Noise includes disturbances in seismic data caused by any unwanted seismic energy, such as shot generation ground roll, surface waves, multiples, effects of weather and human activity, or random occurrences in the Earth. Noise can be minimized by using source and receiver arrays, generating minimal noise during acquisition and by filtering and stacking data during processing."

2.1 Classification of noise

We have two main classes of seismic noise, coherent and random. Coherent noise can be linear or nonlinear depending on type and distance. Random noise is noise that occurs incoherently, for example swell noise.

SI appears as linear coherent noise when it is recorded from long distances, and as nonlinear coherent when recorded from short distances.

2.1.1 Linear coherent noise

Direct wave and refracted wave

The direct wave moves in the form of a straight path along the surface, directly from the source to the receiver as shown in Fig. 1. Refracted waves propagate along the interface between two layers and leak during propagation forming linear events in the seismic data. The condition is that the velocity in the lower layer is highest, as is the case for the seafloor.

In some cases the arrival of refracted waves may be earlier than the arrival of the direct wave. Both of these waves are interfering with our primary reflection data. Typically they are removed by muting for example in τ-p space.

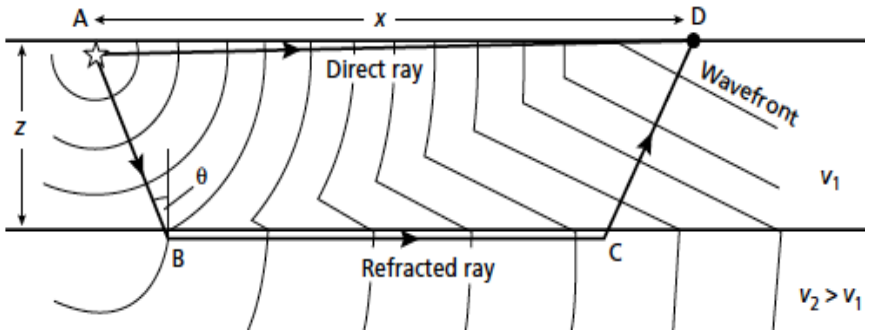

Figure 1: Direct and refracted wave in two layer model (Kearey, 2002).

2.1.2 Non-linear coherent noise

Multiples

Multiples occur when seismic waves are reflected more than once in their travel path by being trapped between two strong reflectors, as in Fig. 2. In marine seismic, typical multiples are water bottom multiples, which represent energy trapped between the sea surface and the sea bottom. These are also known as reverberations. Multiples can have the same arrival time as the primary wave and thus overlap primary data which is something we do not want. They are normally attenuated by various de-multiple methods, e.g. a radon mute.

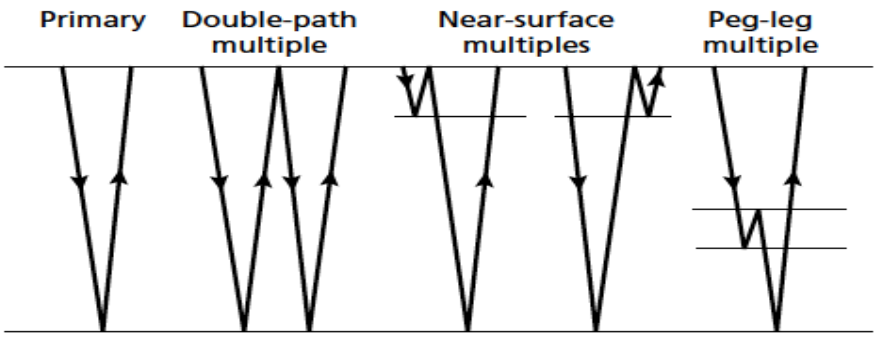

Figure 2: Various types of multiple reflections in a layered ground (Kearey, 2002).

Ghost reflection

The ghost reflection is a special type of multiple reflections, shown in Fig. 3. Part of the energy from the source will propagate upwards and reflect from the sea surface (reflection coefficient close to -1). This is called the source ghost. It recombines with the direct field and defines the effective pulse. A similar phenomenon occurs at the receiver side and is denoted the receiver ghost (see Fig. 3).

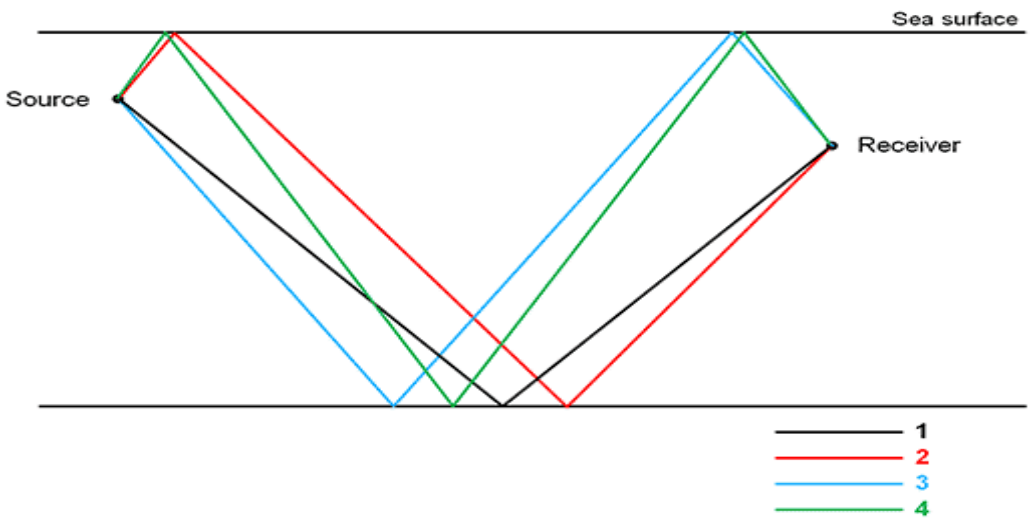

Figure 3: Illustration of ghost (Courtesy of CGG).

In Fig. 3, the black line (1) is the direct wave, the red line (2) is the source ghost and the blue line (3) is the receiver ghost. The green line (4) is the combination of source and receiver ghosts.

Several deghosting technologies have recently been developed for the receiver ghost. The three main technologies are: slanted/multi-level streamers, over-under streamer and dual/multi-sensor.

In dual/multi-sensor towed streamers both hydrophones and velocity sensors are employed. Based on such measurements, the data can be decomposed in upward travelling and downward travelling wave fields by proper combinations (see Fig. 4). Thus the receiver ghost can be efficiently removed.

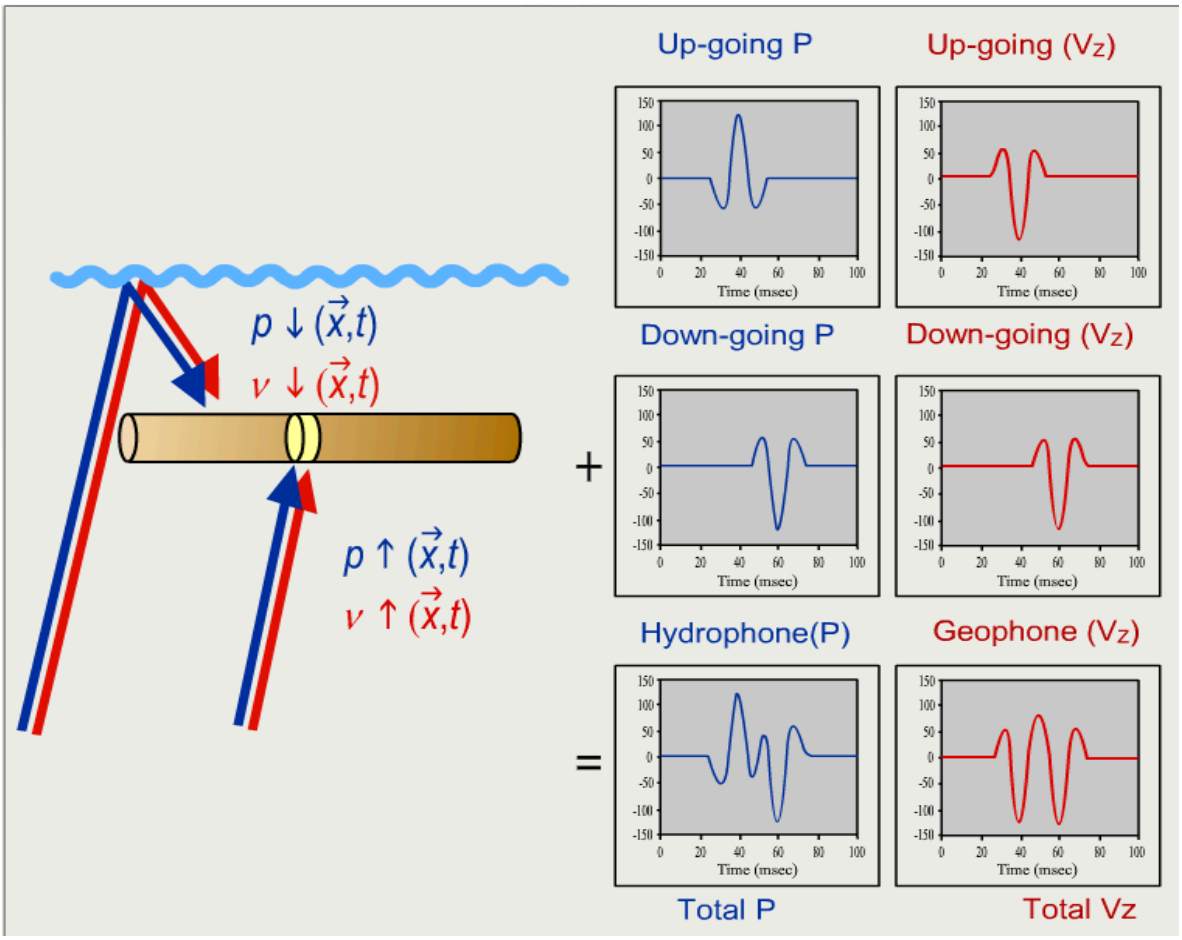

Figure 4: Hydrophone (p) and velocity sensor (v_z) recorded seismic wave field (Gelius and Johansen, 2010).

The over-under technology eliminates the receiver ghost by using information recorded from pairs of streamers deployed at two different depths in the same vertical plane. By using over-under technology we are able to distinguish between the up going and the down going seismic wave fields. We can then remove the down going seismic wave field (ghost) by data processing. We are doing this by adding both streamer outputs to fill the notches in the amplitude spectrum. This method corrects both the phase and amplitude effects of the surface ghost by combining both signals as a weighted sum (Posthumus, 1993), see Fig. 5. This technology is not much in use today due to the difficulties in relation to achieving the accuracy required for this technique to be advantageous. In addition, the over-under technology has proved to be too costly.

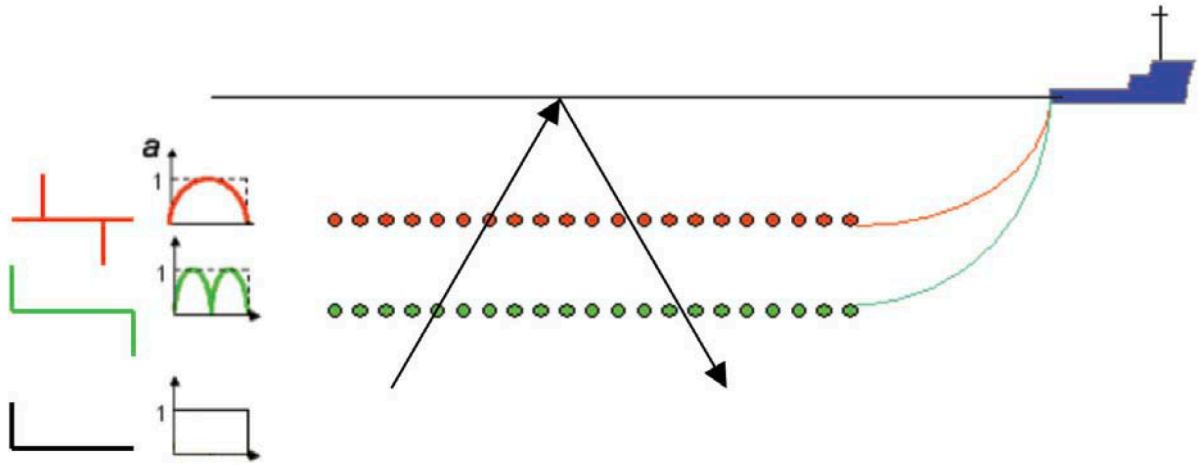

Figure 5: The over/under streamer technology (Moldoveanu et al., 2007).

The slanted/multi-level technology removes the receiver ghost by using information recorded along a variable depth or slanted streamer, see Fig. 6. We can remove the down going seismic wave field (ghost) by exploiting notch diversity along the streamer and stacking this up.

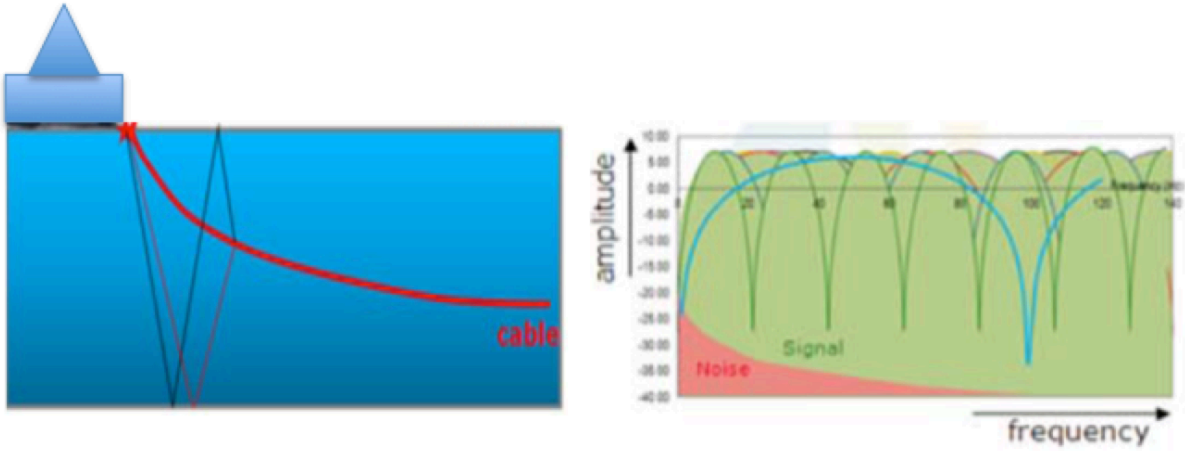

Figure 6: Slanted streamer (left) and notch diversity (right) (Courtesy of CGG).

Deghosting technologies for the source ghost do also exist. One of these technologies is represented by the distributed source. This technology uses sources deployed at two different depths but in the same vertical plane. The two seismic source arrays, which have the same efficiency and density, are fired at different times (generally less than one second delay). Knowing the firing time delay and by proper data processing we can separate the two source wave fields and remove the down going seismic fields (source ghost). By combining both

signals as a weighted sum, similar to the over-under technology, this method corrects both the phase and amplitude effects of the surface ghost (Posthumus, 1993), as illustrated in Fig. 7.

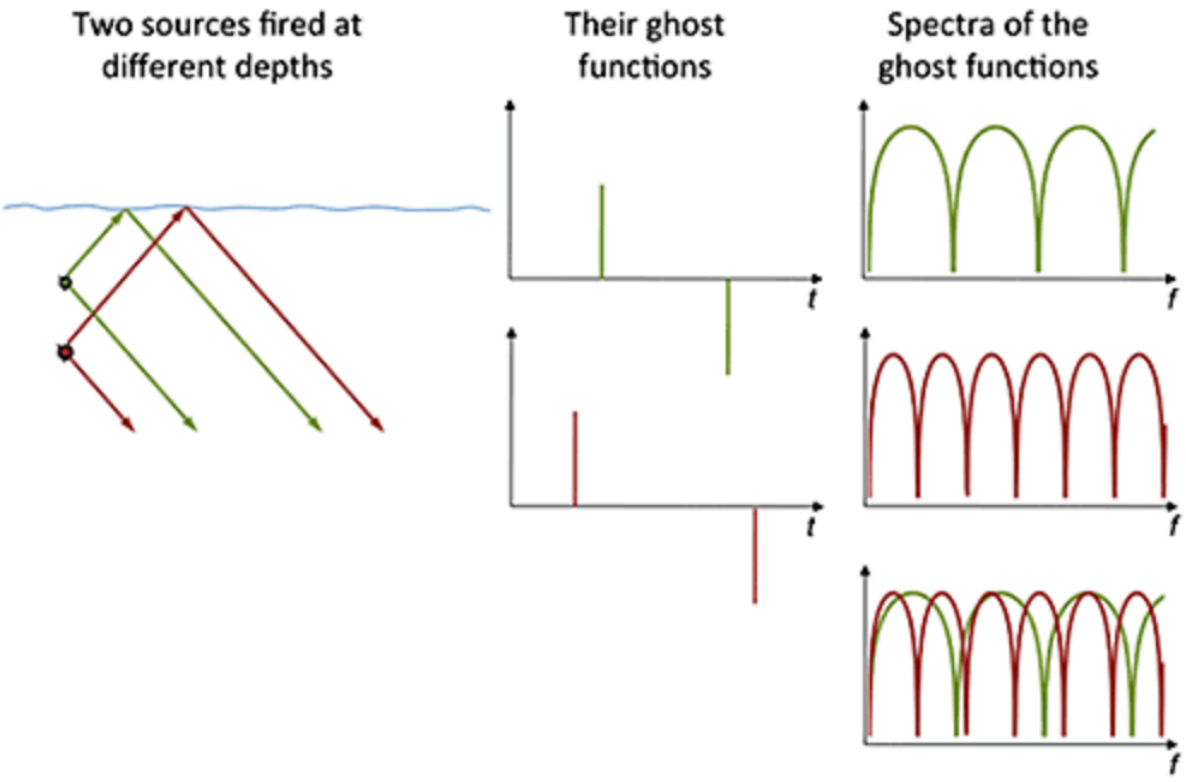

Figure 7: Pairs of source arrays deployed at two different depths and in the same vertical plane (left), primary event and source ghost event (center) and amplitude spectra of these wavelets (right) (Courtesy of www.pgs.com).

Diffraction

When a wave hits a discontinuity e.g. as faults, boulders and other objects, the wave will be scattered and new wave fronts will be created. Such phenomena give rise to a radial scattering of incident seismic energy known as diffraction (shown in Fig. 8). Diffractions appear as hyperbolic or parabolic shaped events in a seismic profile. This type of noise can be challenging to handle in processing.

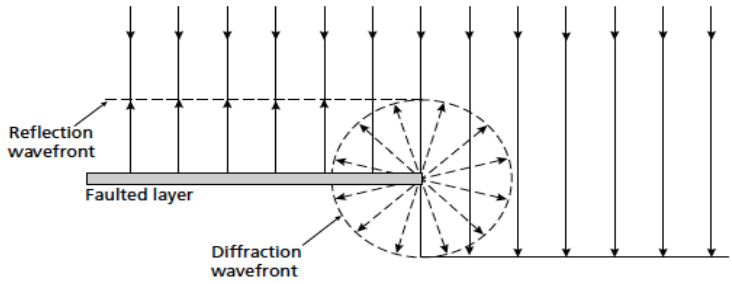

Figure 8: Diffraction at the truncation of a faulted layer (Kearey, 2002).

2.1.3 Random noise

Swell noise

Swell noise represents one type of non-coherent high amplitude noise in the marine seismic environment. It originates from bad weather conditions causing cross-flow over the streamers and induces vibrations in the streamer.

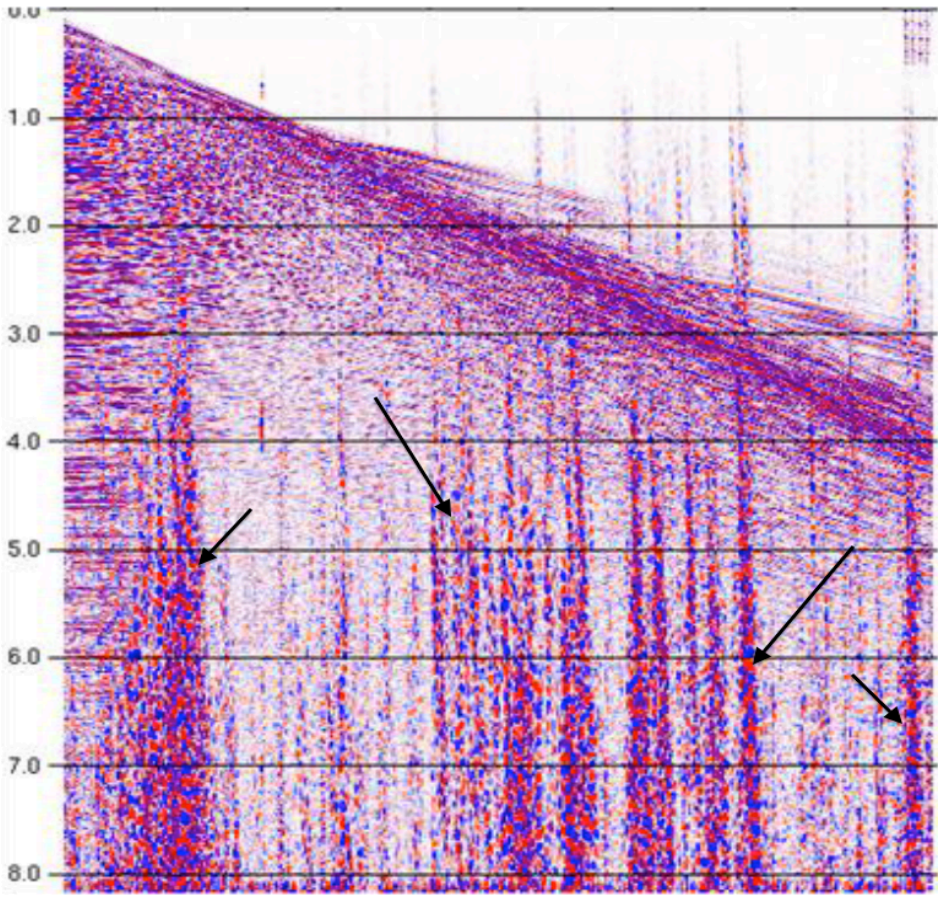

Figure 9: A shot gather with swell noise. The vertical stripes represent swell noise (Presterud, 2009).

Fig. 9 shows a shot gather with swell noise. Swell noise is represented as the vertical stripes on the primary data. Swell noise is interfering our primary data because it has often very high amplitudes at low frequencies and overwhelms the data. Specially designed filters can be employed to attenuate swell noise, e. g. τ-p filter (Jiuying, et al.) and TFDN filter (Presterud, 2009).

Ambient disturbance

Ambient disturbance can occur by natural causes such as rain, wind and tides or from autonomous disturbances as machinery, passing vehicles, etc. Depending on the amplitude of the noise, it has to be attenuated. Fig. 10 shows a more exotic example involving a shark biting the streamer.

Figure 10: Shark biting the receiver cable (Courtesy of CGG).

3. WHAT IS SI AND HOW TO CHARACTERISE IT?

SI is unwanted noise being recorded because of multiple seismic vessels operating in the same area.

3.1 Sound propagation in water

SI is sound propagating in the ocean. The sound level is measured in the decibel scale described by O´Brien (2002):

$$dB = 20 \log_{10}(p/p_0) \tag{3.1}$$

where P_0 is a reference pressure.

The reference pressure in air is 20 µPa and in water 1 µPa chosen to be near the limit of human hearing.

The arrival of SI depends on several factors like distance and direction from interfering vessels to the affected receiver cable and shot intervals of the interfering vessel.

SI decreases with distance because of transmission losses. Calculation of transmission loss in such cases is complicated. Relevant models vary from area to area. Sound propagation is different in the deep ocean than in the shallow water because of the volume (cf. sub-chapter 3.1.1 and 3.1.2).

3.1.1 Sound wave propagation in deep ocean

In deep oceanic water the same energy is spread over a large area and is reduced by the inverse of the square of the distance R, see Fig. 11.

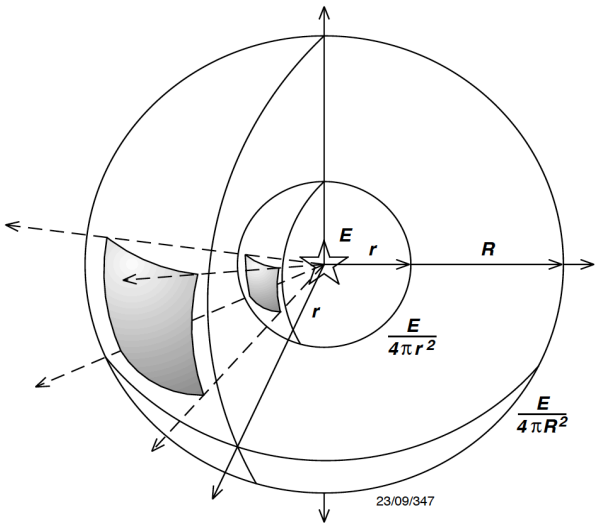

Figure 11: Spherical sound spreading in deep water (O´Brien, 2002).

The sound intensity I will decrease according to a $1/R^2$ relation meaning that the sound pressure reduces according to a 1/R relationship (as $I \sim P^2$) (O´Brien, 2002). From the definition of the decibel scale for pressure, it readily follows that attenuation of sound pressure with distance is equal to $20\log_{10}R$, where R is the distance from the source and assuming a reference pressure measured at a distance of 1 m from the source.

3.1.2 Sound wave propagation in shallow ocean

In shallow water, because of the short distance between sea surface and seabed the sound energy will move along the horizontal direction as guided waves (O´Brien, 2002), see Fig. 12. The short distance between the sea surface and the seabed forms a sound channel with cylindrical divergency and thus a lesser attenuation equal to $10\log_{10}R$ (O´Brien, 2002). The maximum sound level from an airgun falls in vertical direction. Amplitude levels emitted horizontally are normally 20-40 dB lower than those emitted vertically, so smaller amounts of energy can make its way into a sound channel produced by surface stratification (O´Brien, 2002).

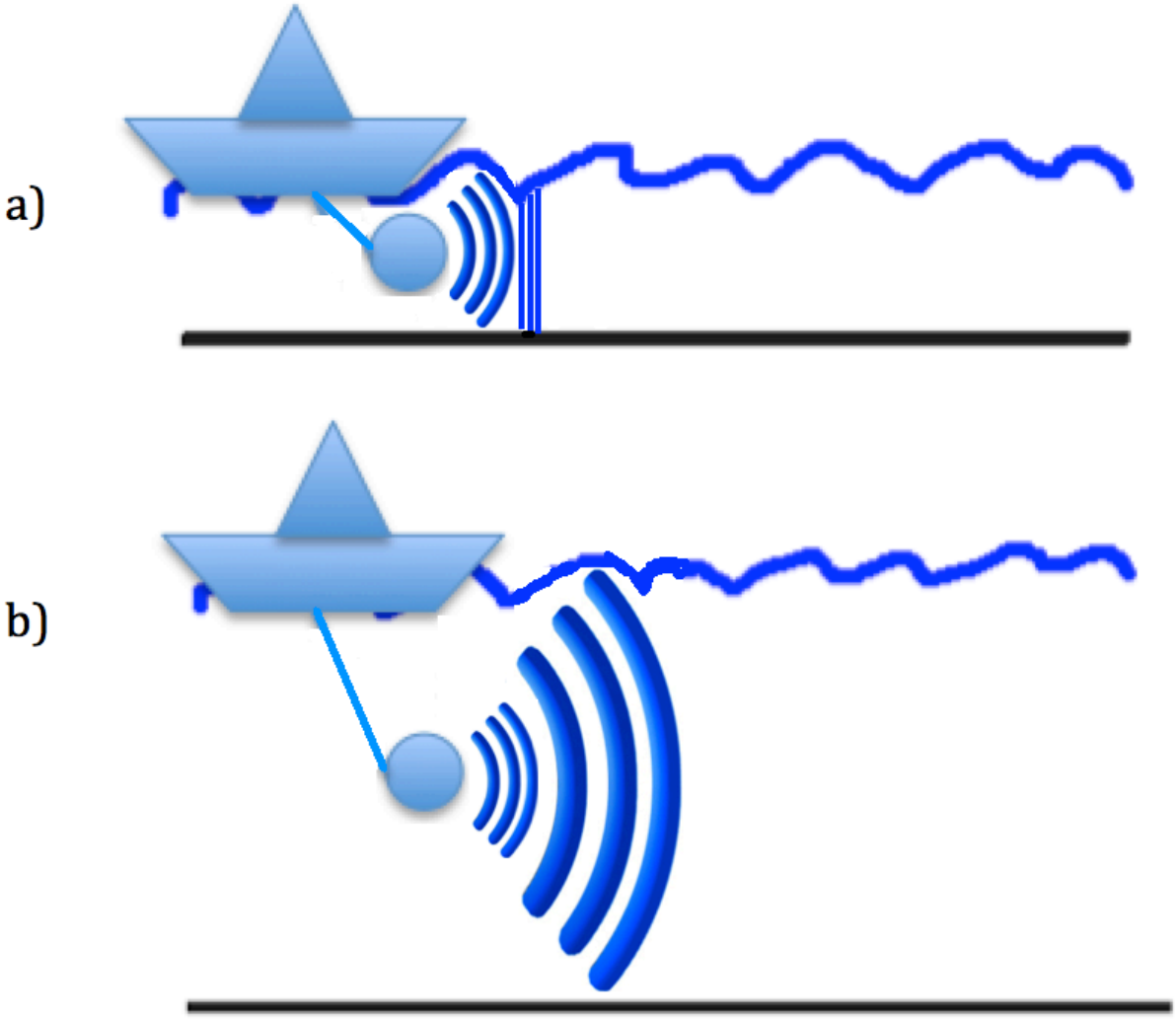

Figure 12: Illustration of sound propagation in shallow water (a) and in deep water (b).

3.2 Arrival and moveout of SI in marine shot gathers

The directions of arrival for SI can be from abeam, astern or from the side of the seismic receiver cables, as illustrated in Fig. 13. SI moves mostly through the water column (Caselitz et al., 2012).

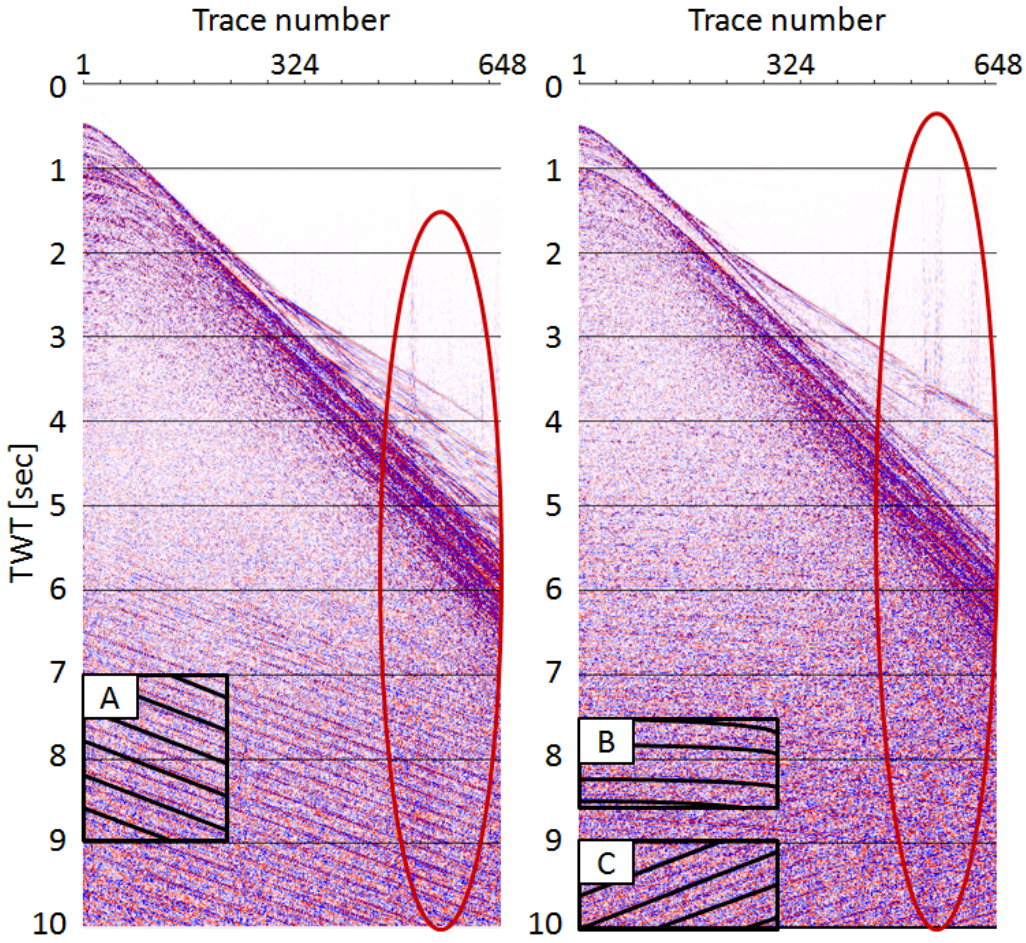

Figure 13: Source gathers with SI (black squares) and swell noise (red circle). SI from abeam (A) is shown on left side. SI form astern (C) and abeam (B) is shown on right side (Jansen, 2013).

The moveouts of SI in a shot gather are defined by the water velocity v, and the angle θ under which the signal arrives at the receiver cable. In sea water the acoustic velocity v may be approximated to $v_w = 1480\ m/s$. The angle θ is varying depending on the direction of arrival. If we assume θ = 0 at inline direction (see Fig. 14), we can define apparent velocity by Jansen (2013) reported that:

$$v_{app} = \frac{v_w}{\cos(\theta)} \tag{3.2}$$

As mentioned earlier, SI appears as linear seismic events if the interfering vessel is far away (> 100km) and appears as curved seismic events if the interfering vessel is close (< 100km). The moveout of SI in a shot gather is defined by (Jansen, 2013):

$$p = \frac{dt}{dx} = \frac{1}{v_{app}} \tag{3.3}$$

The limiting values of the parameters in Eqs. (3.2) and (3.3) are given in Table 1:

Table 1: Limiting values of azimuth angle (green), apparent velocity (black) and slope (red).

$\boldsymbol{\theta}$	$\boldsymbol{v_{app}}$	$\boldsymbol{p}$
0^o	v_w	$1/v_w$
90^o / 270^o	∞	0
180^0	$-v_w$	$-1/v_w$

An illustration of how SI occurs from the side is shown in Fig. 14.

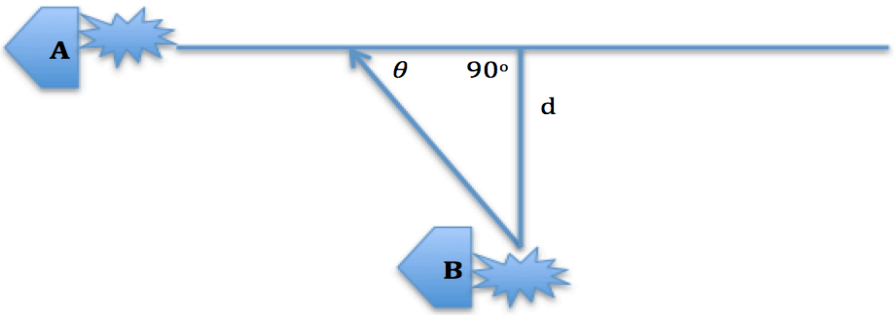

Figure 14: Illustration of SI from the side. SI arriving at the receiver cable associated vessel A, originated at firing air gun of vessel B.

3.3 Frequency spectrum of SI

To characterize seismic noise from marine seismic data we can take a look at the frequency spectrum. If the noise has frequencies which lie outside the frequency range of the seismic

signal, the noise can be removed by using low pass filter, high pass filter or a band pass filter (Gelius and Johansen, 2010).

The seismic source is designed to optimize the frequency band of the seismic data. Normally the frequency band of seismic data falls approximately between 2 – 150 Hz. Thus SI also contains broadband frequencies.

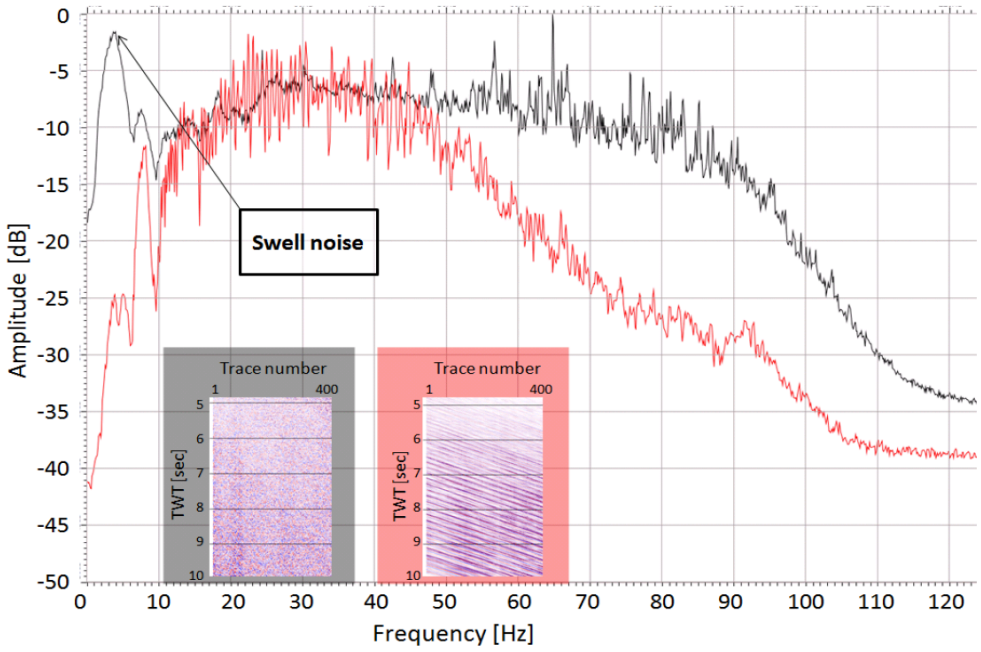

Figure 15: Frequency spectra of SI-free shot gather (black) and pure SI gather (red) (Jansen, 2013).

Fig. 15 shows respectively the frequency spectrum of a SI-free shot gather (black) and the removed SI (red) from the same shot gather. We can see swell noise with high amplitudes at low frequencies (2-6 Hz) in the SI-free shot gather (black). High frequencies are attenuated quicker with distance than low frequencies, which explain why lower amplitudes are observed at higher frequencies of SI than in the actual signal (Jansen, 2013).

Fig. 15 illustrates, the frequency spectrum of the SI-free shot gather and the pure SI gather overlap between 10-50 Hz. Thus SI can not be removed by simple frequency filtering methods because of the overlapping with the primary shot. The solution is to transform and sort these data to make SI randomized. This will be the topic of the next chapter.

4. SI ATTENUATION METHODS

In this chapter different methods of SI attenuating will be discussed.

4.1 Removing SI by using moveout

In general, SI has a different type of moveout compared to the primary data. The following possibilities may occur: same moveout, opposite moveout, horizontal moveout and combination of opposite and same moveout.

The linear Radon transform is also referred to as the τ-*p* transform. SI is usually linear in the shot domain. The τ-*p* method can be used to remove SI if the SI moveout is different from the moveout of the primary data. τ-*p* is a process where data in the space-time domain is decomposed in plane-waves. Each plane wave is represented by a point in the τ-*p* domain where p represents its slope and τ the intercept time at zero offset (Yilmaz, 2001).

When the SI is isolated from the shot gathers two different approaches can be taken to remove the SI from the original data. The first one is to remove SI by muting and the output from this process is a SI free shot gather. However, this method will not fully preserve the signal (Maroof and Gravely, 1984). The other alternative is to choose the SI noises themselves as output, which is then adaptively subtracted from the original shot gather.

When SI has the same moveout as the reflection data we need to sort the data randomly. This again gives the ability to remove SI by using denoising methods that attack random noise.

4.1.1 Randomizing

As mentioned in chapter 3, SI often appears as linear coherent noise in the shot domain. This property of SI can change from coherent noise to random noise by proper sorting of data.

Three common sortings of consecutive shot gathers are discussed to ensure a random appearance of SI:

- Common offset domain
- Common midpoint domain (CMP)
- Common-*p* domain

Once data is sorted, we can remove SI by random noise attenuation methods.

Common offset domain

In this domain all traces have the same offset. It means we do not have a varying distance between source and receiver. The number of common offset gathers in marine seismic data corresponds to the number of channels. One common offset gather corresponds to data selected from one channel. An example of data sorting to common offset domain is shown in Fig. 16.

In the Uniseis software we are sorting shot gathers by using the program THSORT (trace-sorting).

To obtain the result in Fig. 16 the sorting parameters shown in Table 2 are used.

Table 2: Parameters used to sort data to common offset domain.

ITRNO
ICDP

The parameters in Table 2 represent:

- ITRNO: Primary key to sort on (e.g. trace number).
- ICDP: Secondary key to sort on (e.g. CDP number).

In order to generate a common-offset section, ITRNO is fixed and ICDP is varying over the CDP-range.

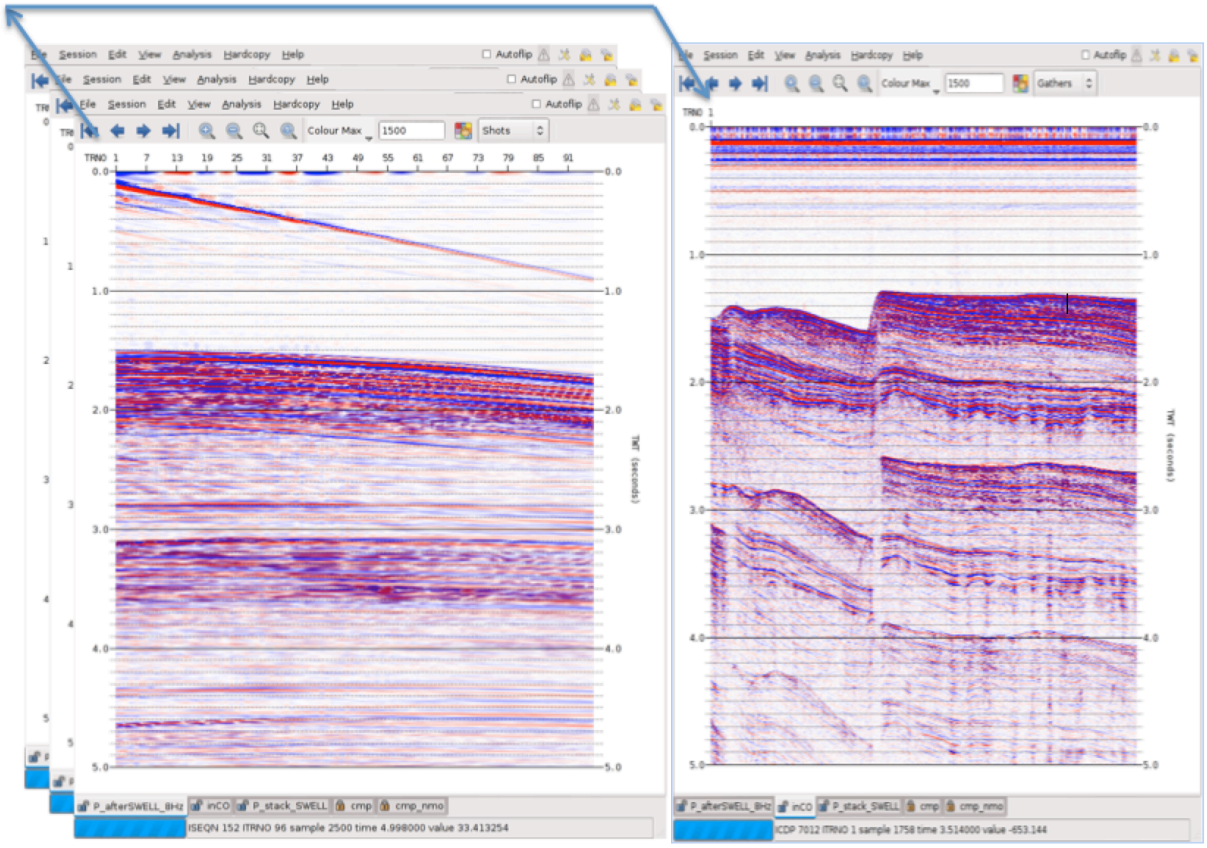

Figure 16: Sorting to common offset domain. Shot gathers (left) and common offset domain (right).

The common-offset section corresponds here to the nearest trace. We have a complex geology in this area and a set of fractures can be seen in the common offset domain.

Common midpoint domain (CMP)

CMP is a collection of traces sharing the same midpoint. A CMP coincides with common depth point (CDP) only for a horizontally layered earth, as shown in Fig. 17 (a). The more realistic case of a dipping layer is illustrated in Fig. 17 (b).

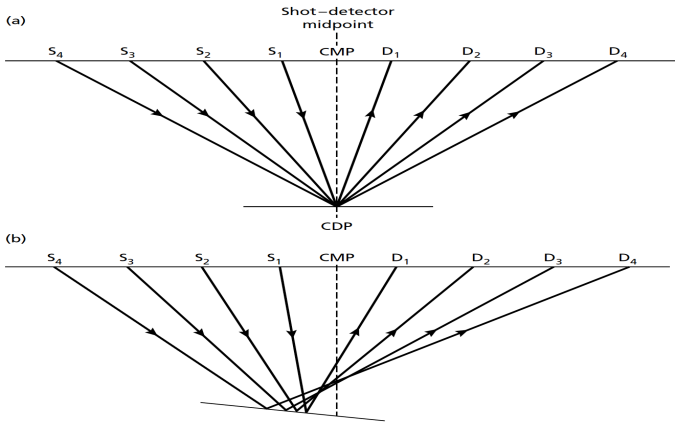

Figure 17: Sorting of data in CMP. (a) Reflections from common depth point (CDP) in case of a horizontal reflector. (b) Different reflection points in case of a dipping layer (Kearey, 2002).

The multicomponent data employed in this thesis were acquired using a cable with 96 channels, a group interval of 12.5 m and a shot interval of 50 m. Therefore, the fold of the data is only 12 in this case which follows from the formula:

$$F = \frac{N\Delta g}{2\Delta s} \tag{4.1}$$

where N is the number of hydrophones, Δg is the group interval and Δs is the shot point interval.

The CMP sorted data is shown in Fig. 18. We sorted the shot gathers using the MSORT module which means regular sorting of marine shot ordered data to CMP sorted format.

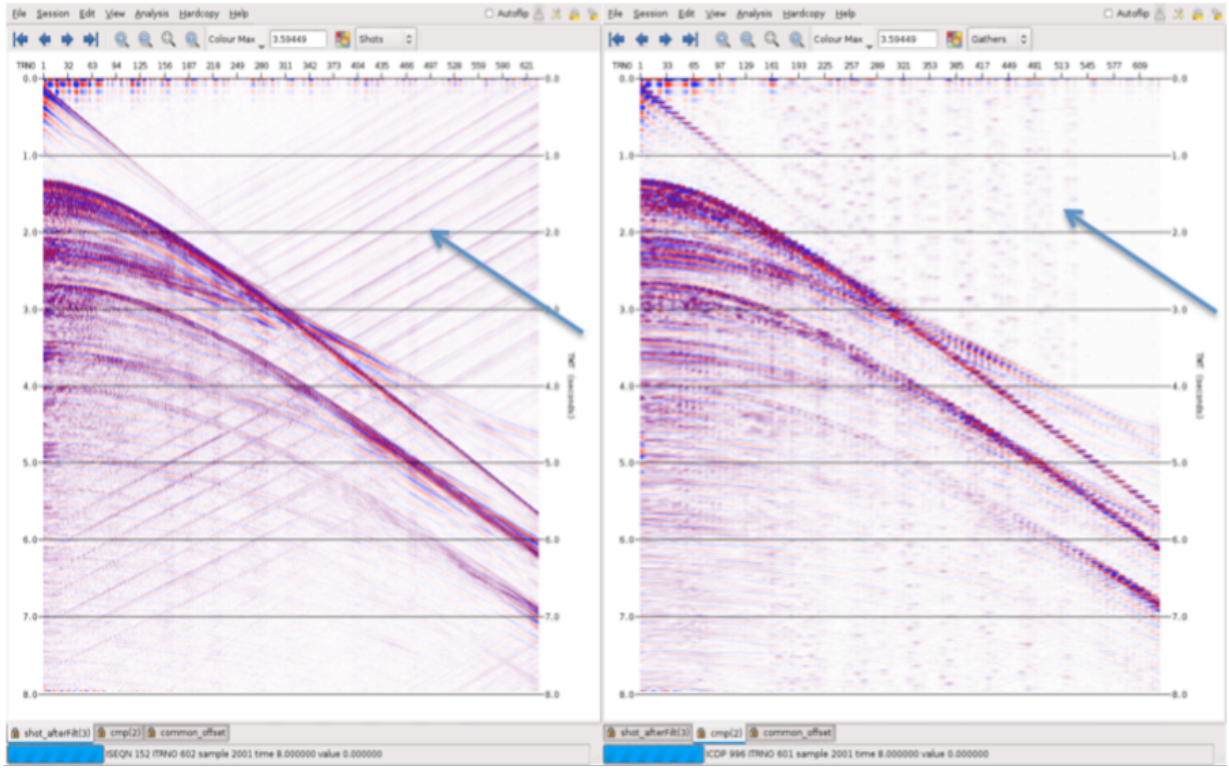

Figure 18: Shot gather (left), CMP (right).

Common-*p* domain

Sorting in the common-*p* can also be used to remove the SI. This method was first introduced by Elboth and Hermansen (2009) and is the one employed in this thesis work.

It involves data from shot gathers being transformed to the τ-p domain. The number of obtained τ-*p* gathers corresponds to the number of transformed shot gathers. The number of common-*p* gathers is determined by the total p-traces that exist in each τ-p gather:

$$\text{Number of common} - \text{p gather} = \frac{(\text{DTmax} - \text{DTmin})}{\text{DT}} + 1 \qquad (4.2)$$

where DT_{min} and DT_{max} represent the moveout range in each τ-p transform, and DT represent the moveout increments within the range.

The common-*p* domain is shown in Fig. 19. To obtain this result the following parameters were set to do the τ-p transformation:

Table 3: τ-p parameters used for shot gathers.

OPUT	TAUP
PATH	LIN
DELT	DTmin, DTmax, DTinc
XREF	dfar

Parameters in Table 3 represent:

- OPUT = specifies what type of ensemble to output to the next UNISEIS phase.
- TAUP = pass on the τ-*p* transform data (with padding and appended synthetic data). The trace length will be increased. Do a check run to get padding and new trace length values.
- PATH = can be used to specify the form of the moveout path for which the transform is designed. In addition to linear moveout (τ-*p*), a parabolic moveout is also available (Radon).
- LIN = use linear moveout alignments (τ-*p*)
- DELT = specifies the list of τ-*p* traces which are to be created, defined by their far trace residual moveout (Delta-Time).
- DTmin = minimum delta-times (ms) of τ-*p* traces which is defined at the furthest offset.
- DTmax = maximum delta-times (ms) of τ-*p* traces which is defined at the furthest offset.
- DTinc = delta-time increment between τ-*p* traces.
- XREF = the offset at which the delta times values on the DELT card apply. This should be set to the largest far trace offset that occurs on the line.
- dfar = distance from source to far trace in meter.

After τ-p transformation of the shot gathers, data are sorted into common-*p* gathers using the parameters in Table 4.

Table 4: Sorting to common-p parameters.

SORT	ITRNO. ISEQN, 4, Ptraces
OPTN	-2

The parameters in Table 4 represent:

- SORT = specifies sorting keys.
- OPTN = sorting options.

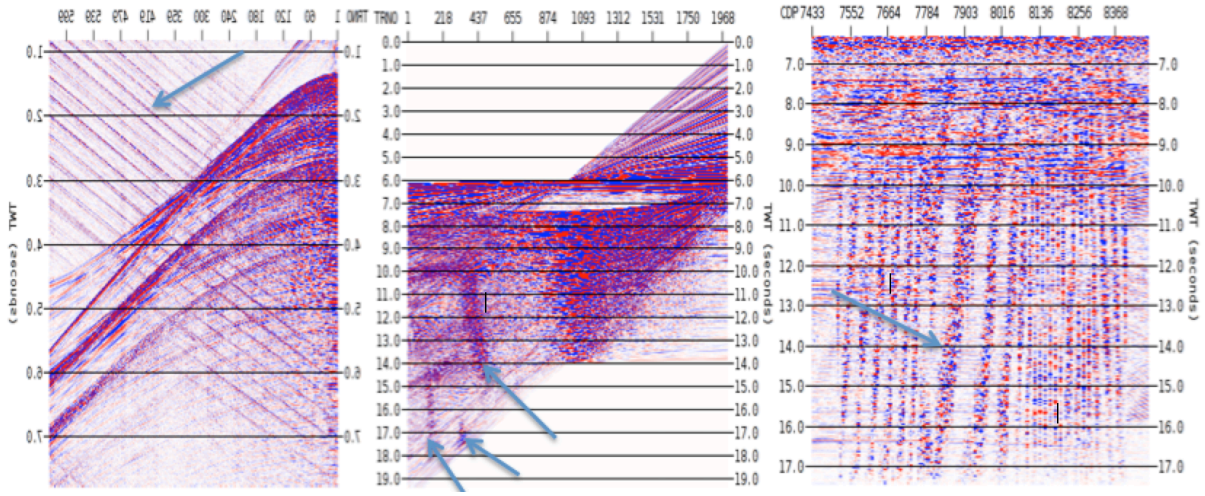

Figure 19: Shot gather (left), same gather in the τ-p domain (center) and the common-p domain (right). SI is shown by blue arrow and is randomized as vertical stripes in the common-p domain.

It can be seen from Fig. 19 that SI (shown with arrow) is now randomized in vertical stripes in the common-*p* domain.

4.2 Random noise attenuation

The aim of sorting data from shot gathers to a more proper domain is to randomize the SI. Such randomized SI can now be removed by various techniques as described below.

4.2.1 Time Frequency De-Noising (TFDN)

TFDN is known to be an efficient method to remove random noise while preserving the signal. A similar method like TFDN was first presented by Vassilious and Garossino (1998). An improved version of this implementation was published by Elboth et al. (2008), and later applied in the common-p domain to attenuate SI (Elboth and Hermansen, 2009).

TFDN starts by choosing a window w_n of data, which is transformed from time to frequency domain using Fast Fourier Transform (FFT)[1]. The amplitudes a (w_n, f, x) of each frequency are sorted from the smallest to the largest. The median is used as a threshold thr (w_n, f, x) to reduce amplitudes that are anomalously high. Finally, an inverse FFT takes the filtered result back to the time domain.

This procedure is shown schematically in Fig. 20.

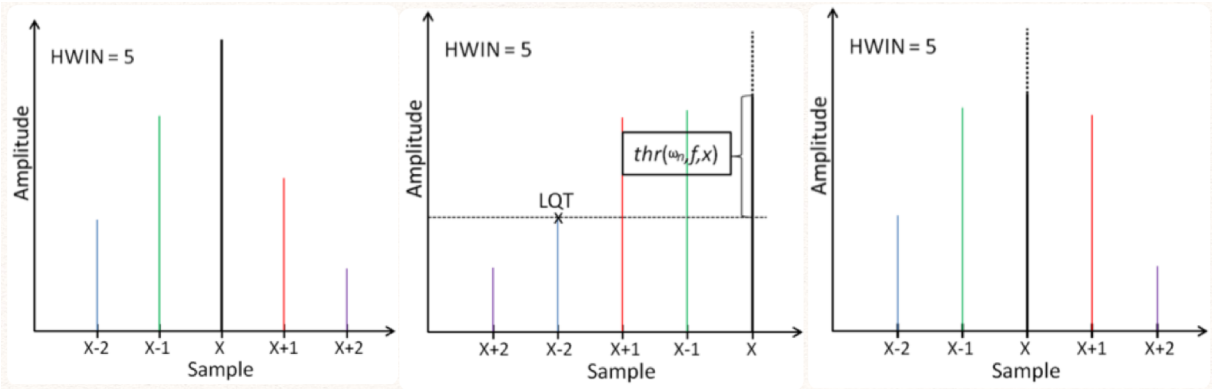

Figure 20: Amplitude samples (left) with center amplitude X, sorted in ascending order (center), and muting X according to threshold, finally sorting back (right).

To calculate the threshold we multiply a user defined time-dependent factor fac (t) with the amplitude of an almost noise free trace. The noise free trace can correspond to the median (MED), the average (AVR), or the lower quartile (LQT) within the window HWIN. If less than 50% of the HWIN traces are affected by SI, we can use median (Presterud, 2009). If more than 50% of the HWIN traces are affected by SI, we can use lower quartile estimation (Presterud, 2009).

The definition of the median and the lower quartile are:

$$MED(x) = median(x) = \frac{number\ of\ values\ in\ the\ array+1}{2} \tag{4.3}$$

[1] A Fast Fourier Transform (FFT) is an algorithm to compute the discrete Fourier transform (DFT) and its inverse. Fourier analysis converts time (or space) to frequency and opposite. An FFT rapidly computes such transformations by factorizing the DFT matrix into a product of sparse (mostly zero) factors (Gelius and Johansen, 2010).

$$LQT(x) = Lower\ quartile(x) = (number\ of\ values\ in\ the\ array + 1) * (\frac{25}{100}) \quad (4.4)$$

Assuming that the median is used, TFDN can identify and attenuate high amplitudes at the considered frequency f in HWIN according to the following relation:

$$a(w_n, f, x) = \begin{cases} thr(w_n, f, x) & if \quad a(w_n, f, x) > thr(w_n, f, x) \\ a(w_n, f, x) & if \quad a(w_n, f, x) \leq thr(w_n, f, x) \end{cases} \quad (4.5)$$

with thr (w_n, f, x) = MED (x) * fac (t). This process is repeated for all frequencies specified by the user. Finally, an Inverse Fast Fourier Transform (IFFT) brings the modified amplitude spectrum back to time domain. The process is repeated for the central trace in each sliding window.

The result of TFDN filtering is displayed in Fig. 21 on a gather with swell noise. In general the TFDN algorithm works well in attenuating seismic noise. However, in this case a residual amount of data has been removed (upper part in difference plot).

To obtain the result in Fig. 21 the following parameters were used:

Table 5: Parameters used to do TFDN filtering. Starting from 200 s TWT.

TIMR	200
FREQ	0 – 30
HWIN	29
THRS	MED, 4, 3
TWIN	500 - 20

Table 6: Parameters used to do TFDN filtering after 2500 s TWT.

TIMR	2500
FREQ	0 – 15
HWIN	29
THRS	LQT, 3, 2
TWIN	500 - 20

The TFDN filtering started from 200s (TWT). From 2500s and downward lower frequencies were selected and LQT as threshold, because parts of the signals were absorbed by the Earth.

The actual parameters in Tables 5 and 6 represent:

- TIMR = start time of TFDN processing in ms.
- FREQ = frequency, start and end frequency for processing in frequency domain (Hz).
- HWIN = horizontal window length in number of traces.
- THRS = threshold, defines the type of attribute to be used for threshold calculation and factor to determine the threshold at the start and end time of processing.

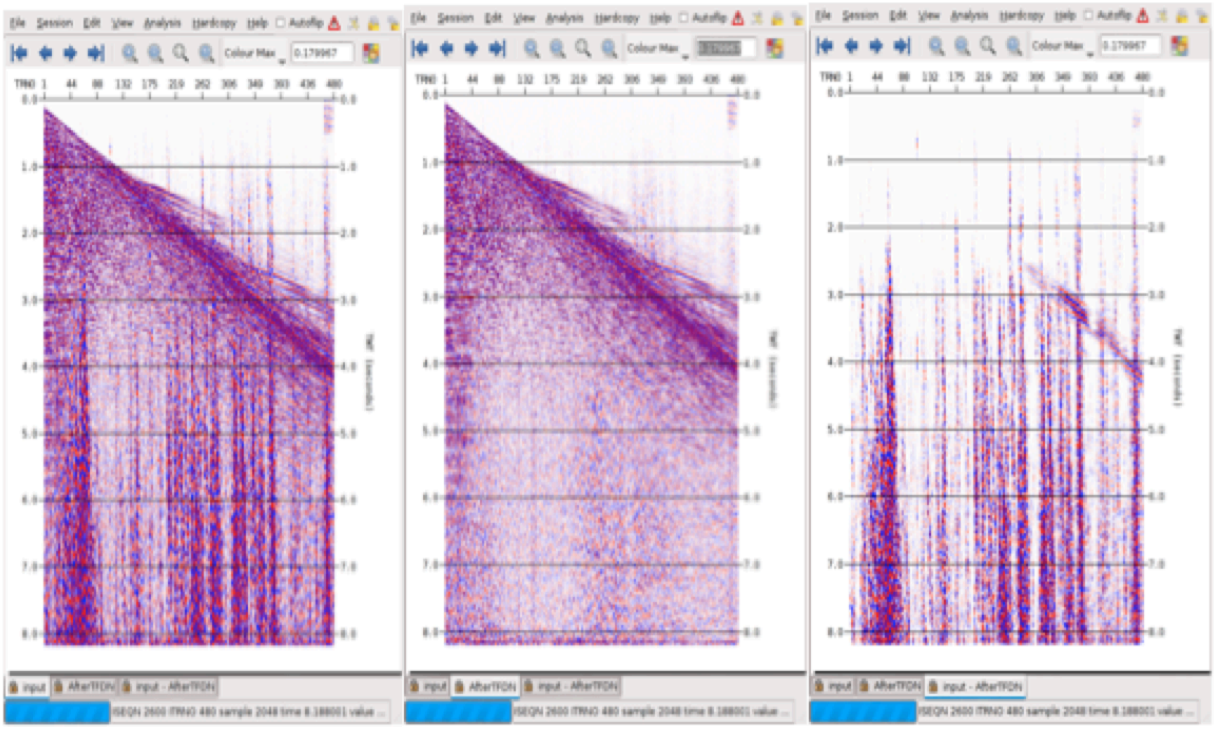

Figure 21: Original data (left), result after TFDN filtering (center) and the difference (right).

4.2.2 f-x Prediction Filtering (f-x PF)

F-x PF was first introduced by Canales (1984).

The basic assumption behind this technique is that we have some kind of linear moveout in our data. By dividing the seismic section into overlapping windows, this assumption may be locally valid. This method is known to work well for random noise attenuation, but is not

amplitude preserving. The underlying assumption of local linear events can be a problem to fulfill in areas of complex geology.

F-x prediction filtering is mostly applied to seismic data, at large recording times, where the interfering noise shows higher amplitudes than the underlying possible reflections.

The following derivation of f-x PF is based on the presentation given by Presterud (2009). Consider a linear event in space and time:

$$f(x,t) = \delta(a + bx - t) \tag{4.6}$$

where δ is the delta-function. Next, take the Fourier transform with respect to time:

$$f(x,\omega) = e^{i\omega(a+bx)} \tag{4.7}$$

Introduce now trace sampling with spacing Δx:

$$u_n = f(x_n,\omega) = e^{i\omega(a+bn\Delta x)}, \qquad n = 1,2,\ldots,N \tag{4.8}$$

where N represents the total number of traces considered. From Eq. 4.8 it follows that:

$$u_n = \alpha u_{n-1} \quad , \quad \alpha = e^{i\omega tb\Delta x} \tag{4.9}$$

which states the essence of f-x PF with the data point u_n being predicted from the previous point u_{n-1}. Unwanted values as random noise can therefore be identified and removed. We have to ensure that the event is based on the underlying assumption that the amplitude of SI is higher than the amplitude of the underlying signal (Gulunay, 2008).
The result from f-x PF filtering is shown in Fig. 22. In general the f-x PF algorithm works well in attenuating seismic noise, but does not work well here to remove SI.

To obtain the result in Fig. 22 the following parameters were employed:

Table 7: Parameters used to do f-x PF filtering.

FILT	9, 96, 20
WIND	200, 8000
OPTN	1

Parameters in Table 7 represent:

- FILT = specifying the filter: filter length, number of traces in each block, white noise percentage.
- WIND = specifies the time window over which noise rejection filtering will performed (minimum and maximum scale).
- OPTN = parameter specifies which output from the filtering process is desired, the filtered data or the removed noise.

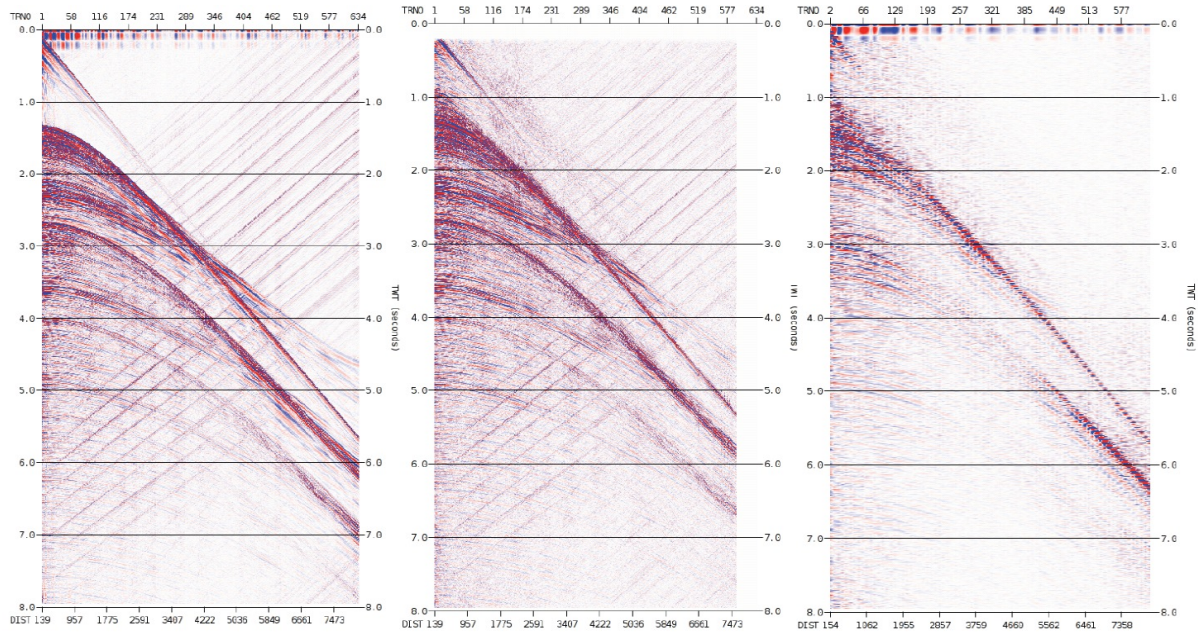

Figure 22: Original data to the left, after f-x filtering to the right and the difference in the center.

The f-x PF was run directly on data (shots) in the inline direction, but the result is unsatisfactory (see Fig. 22). The reason is the moveout of data. Although the SI is linear, the data generally have dip.

Alternatively, one may have tried filtering along the crossline direction and performing NMO corrections to obtain better results, but it will need very high computational times.

4.2.3 τ-p transformation

The τ-p transformation decomposes data in the space-time domain into plane waves. Each such plane-wave follows a linear phase:

$$\tau = t - px \tag{4.10}$$

where p is the ray parameter or slope of the plane-wave, x is the offset, t is the two-way travel time, and τ is the intercept time of the plane-wave at zero offset.
The actual (τ-p) transformation is carried out by the following summation over offset of input data $P(x,t)$ (Yilmaz, 2001).

$$S(p,\tau) = \sum_x P(x, \tau + px) \tag{4.11}$$

where S (p, τ) represents a plane wave with ray parameter p = sin θ/v.
Repeating this calculation for a range of p and τ values, a τ-p gather is constructed.

All traces in a shot gather are decomposed into a series of straight lines that map to points in the τ-p domain, as shown in Fig. 23. Hyperbolic events are shown as elliptical curves in the τ-p domain (Excess Geophysics, www.xsgeo.com).

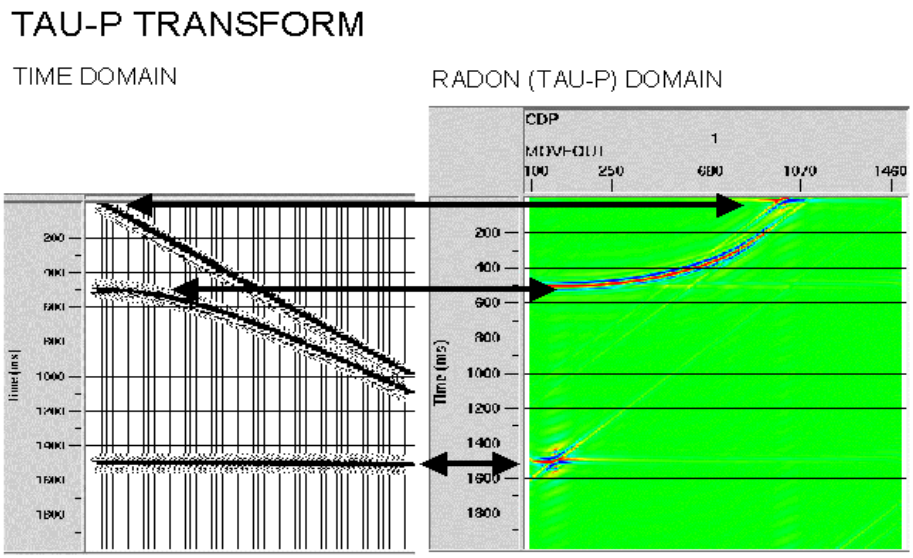

Figure 23: Schematic of τ-p transformation (Excess Geophysics, www.xsgeo.com).

Like in the case of Fourier Transform, an inverse (τ-p) transformation exists that takes data back to the space-time domain. When transformed to the τ-p domain, SI will often map into areas that can be muted except for cases where SI and the seismic signals have similar or overlapping move-out (Elboth and Hermansen, 2009). Fig. 24 shows the results of forward and inverse (τ-p) transformation of a shot gather.

The results in Fig. 24 were obtained using the following parameters:

Table 8: Forward τ-p parameters used for shot gather.

OPUT	TAUP
PATH	LIN
DELT	DTmin, DTmax, DTinc
XREF	dfar

Table 9: Inverse τ-p parameters.

OPUT	TOFF
PATH	LIN
DELT	DTmin, DTmax, DTinc
XREF	afar

Parameters in Table 8 and 9 represent:

- OPUT = specifies what type of ensemble to output to the next UNISEIS phase.
- TAUP = pass on the τ-*p* transformed data (with padding and appended synthetic data). The trace length will be increased. Do a check run to get padding and new trace length values.
- TOFF = pass on the normal time-offset domain data. Input is assumed to be τ-*p* data. (Padding and synthetic data is removed).
- PATH = can be used to specify the form of the moveout path for which the transform is designed. In addition to linear moveout (τ-*p*), a parabolic moveout is also available (Radon).
- LIN = use linear moveout alignments (τ-*p*)

- DELT = specifies the list of τ-*p* traces which are to be created, defined by their far trace residual moveout (Delta-Time).
- DTmin = minimum delta-times (ms) of τ-*p* traces which is defined at the furthest offset.
- DTmax = maximum delta-times (ms) of τ-*p* traces which is defined at the furthest offset.
- DTinc = delta-time increment between τ-*p* traces.

- XREF = the offset at which the delta time values on the DELT card apply. This should be set to the largest far trace offset that occurs on the line.

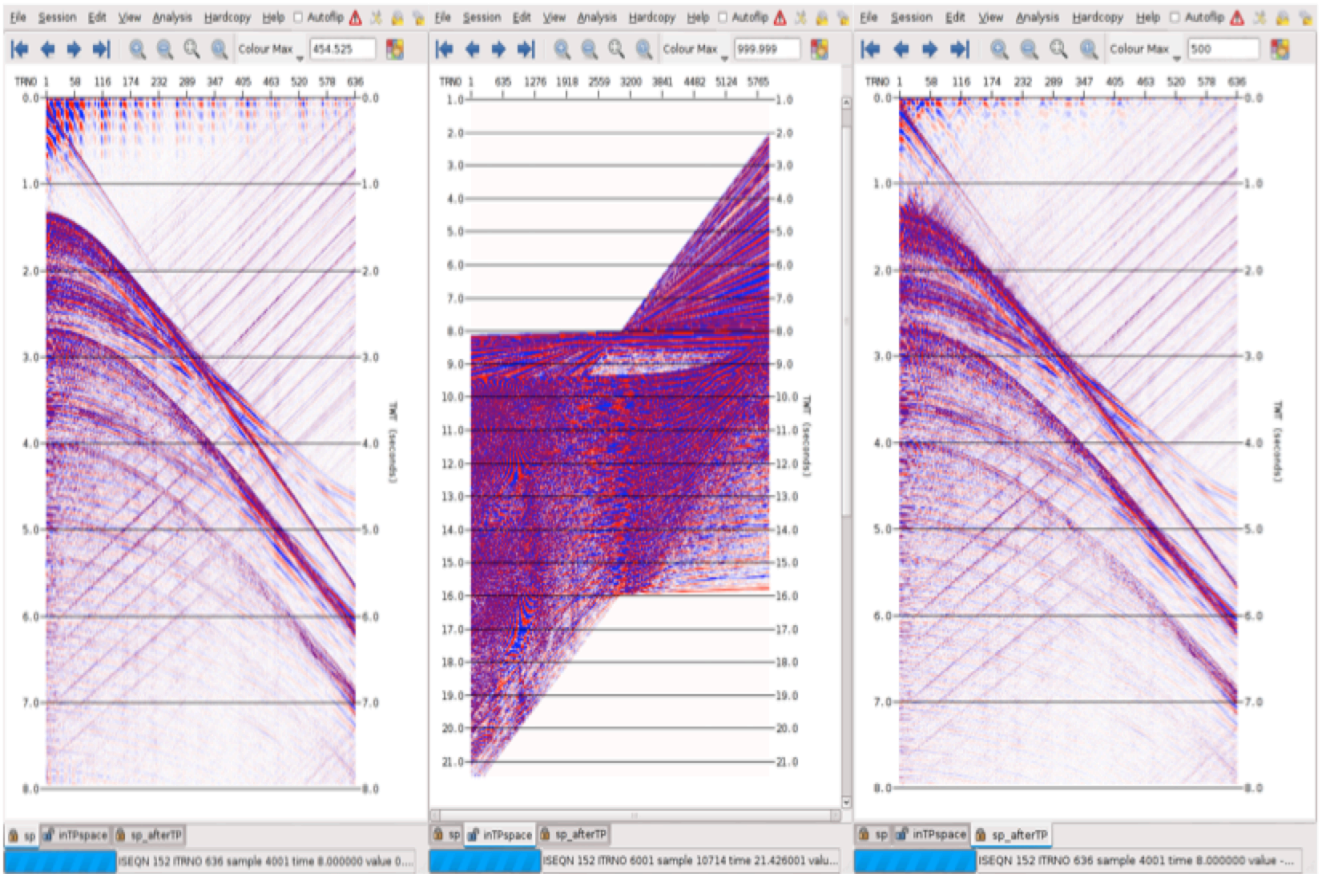

Figure 24: Forward and inverse τ-p transformation. Shot gather (right), τ-p domain (center) and pseudo shot gather after inverse τ-p (right).

In a standard implementation of the forward and inverse $(\tau\text{-p})^{-1}$ transformations, the combined use of them as in Fig. 24 gives an output slightly different from the input. This is due to incomplete amplitude factors.

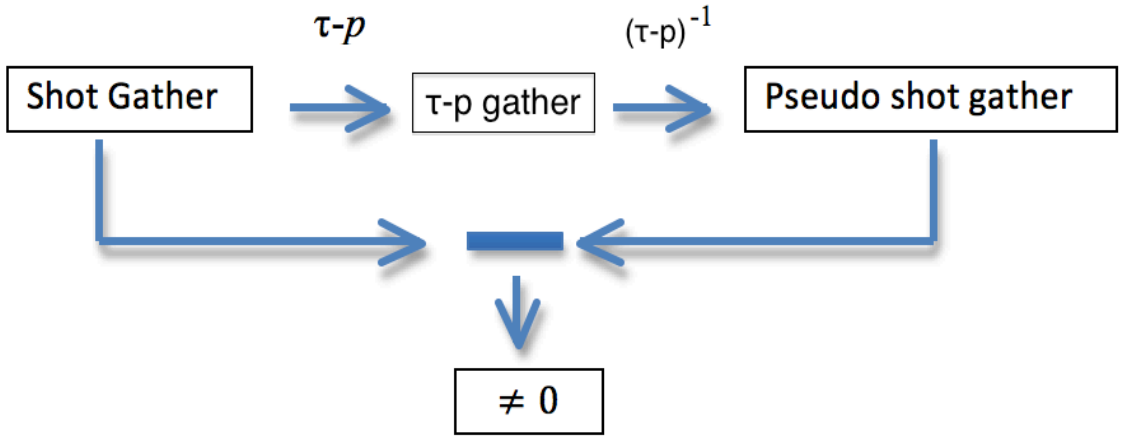

Figure 25: Schematic illustration of transformation from shot gather to τ-p followed by inverse τ-p to shot gather (pseudo).

5. PROCESSING STRATEGY

Based on initial testing of various approaches as described in chapter 4, the τ-p to common-p method (cf. Elboth and Hermansen, 2009) was used in this thesis. A schematic illustration of the τ-p to common-p method is given in Fig. 26 below:

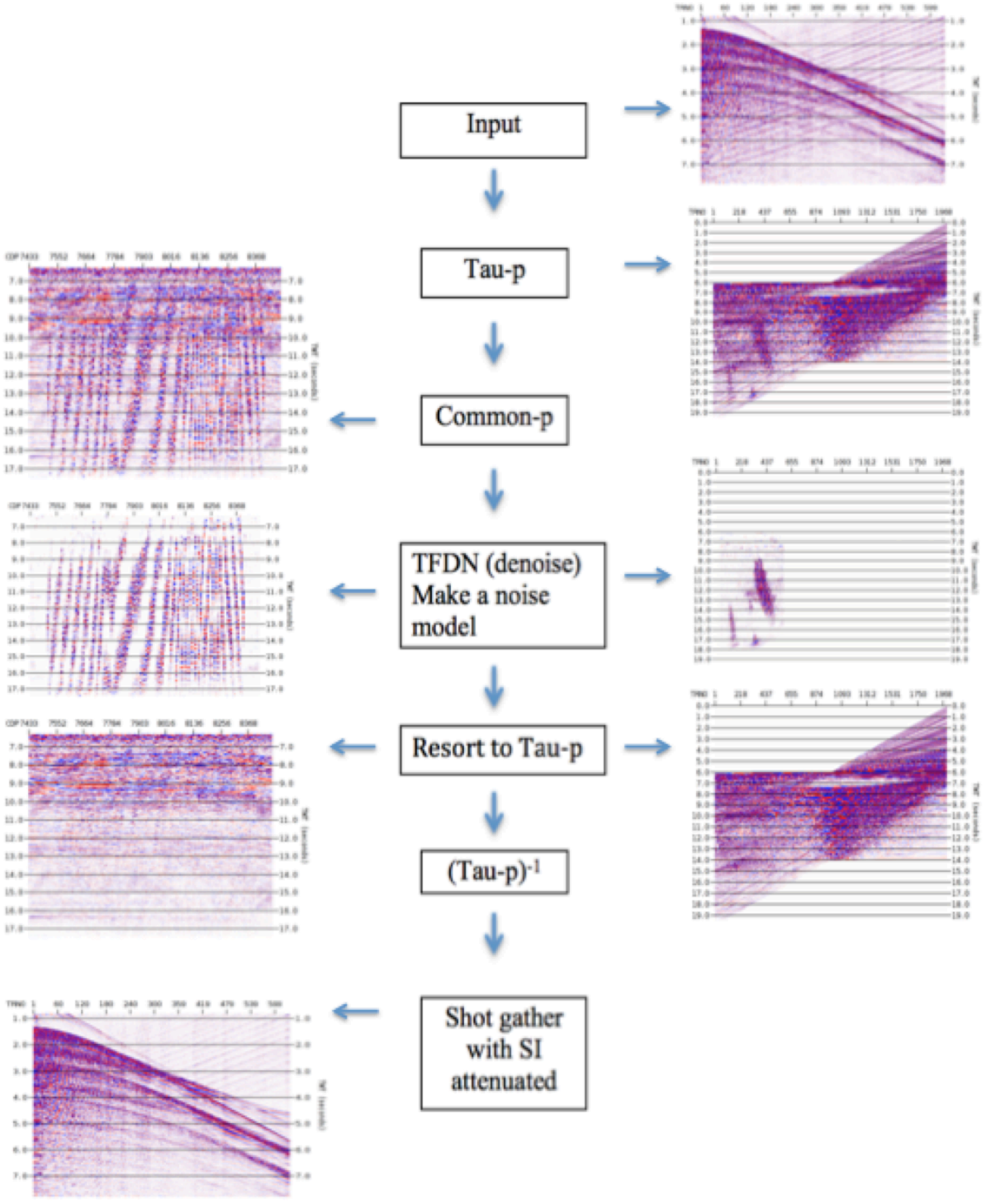

Figure 26: Schematic illustration of the τ-p to common-p method.

The τ-p to common-*p* technique can be divided into these main steps:

1. Transformation of shot point data to the τ-*p* domain.

   Fig. 27 shows a typical example of a (*τ*-p)-transformed source gather. During this processing the same parameters as introduced in section 4.2.3 were employed.

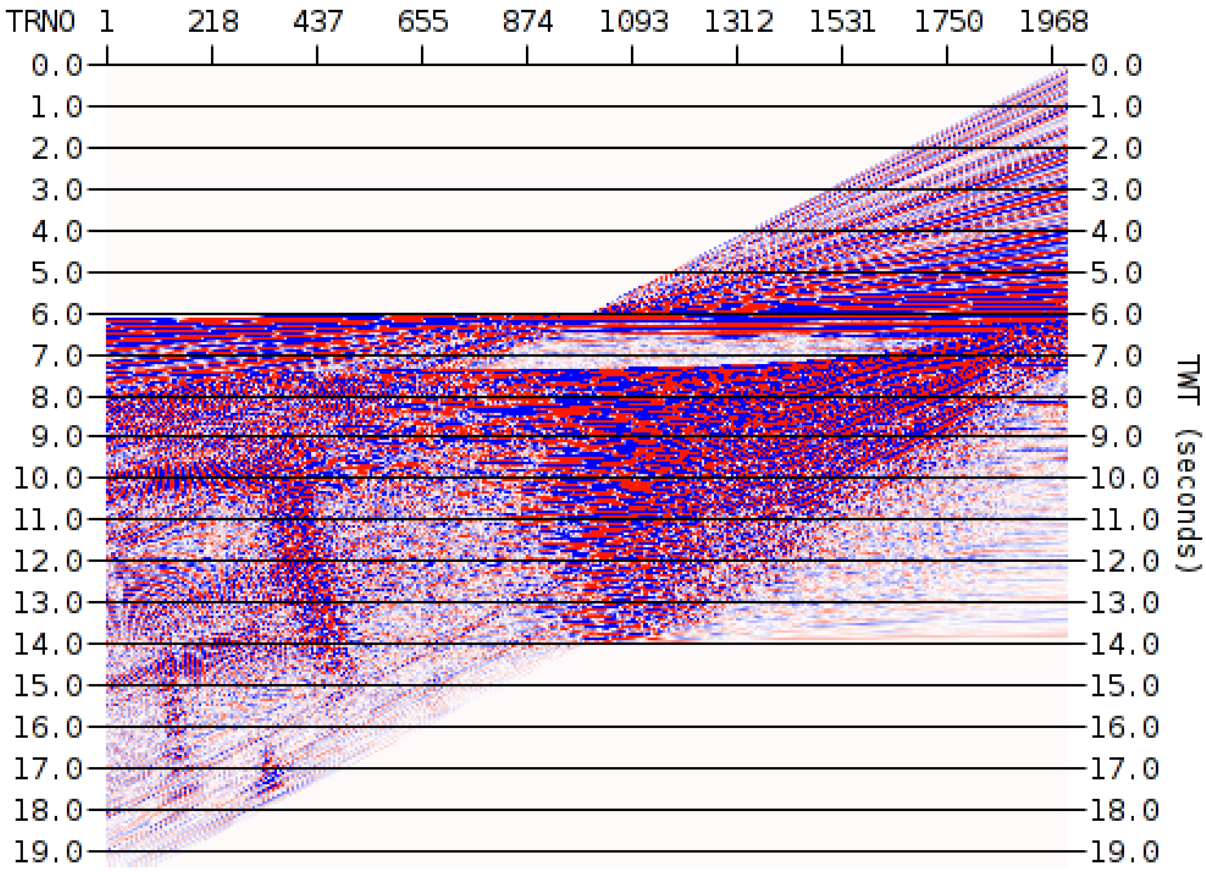

Figure 27: τ-p transformation of source gather.

2. Sort to common-*p*

   In the second step we sort the (*τ*-p)-transformed data to common-*p*. SI is now randomized and it is easier to attenuate it by using standard denoising tools. The data can then be filtered using TFDN. Fig. 28 shows the corresponding results.

These processing steps were performed using the same parameters as in sections 4.1.1 and 4.1.2.

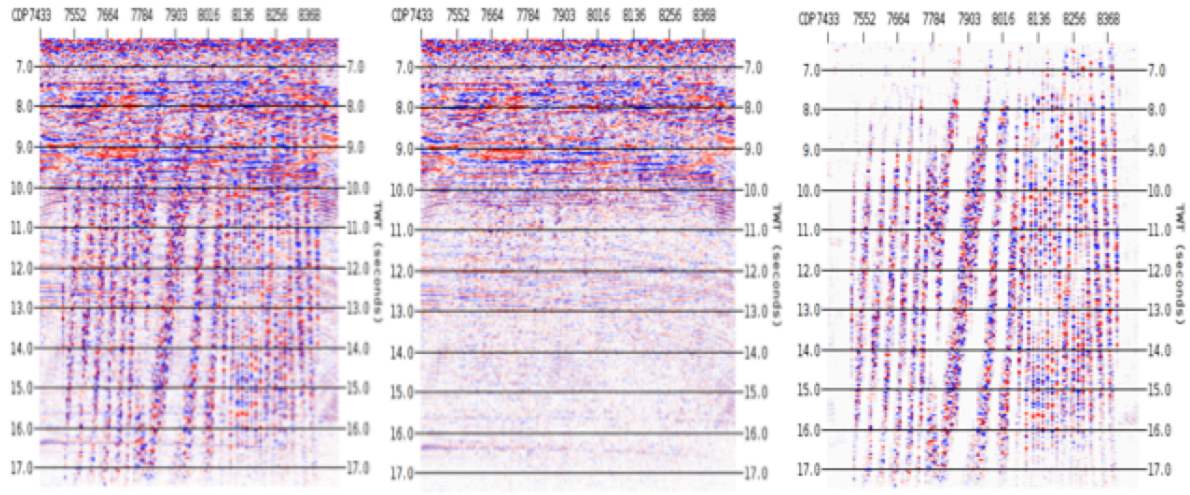

Figure 28: The common-p job. SI is randomized (right), SI is removed (center), the difference (left).

3. Sorting back to τ-*p*

   The TFDN-filtered data will be subsequently sorted back to (τ-p)-gathers.

   Fig. 29 displays an example of the same (τ-p)-gather as in Fig. 28 after such filtering (left) and the difference (right).

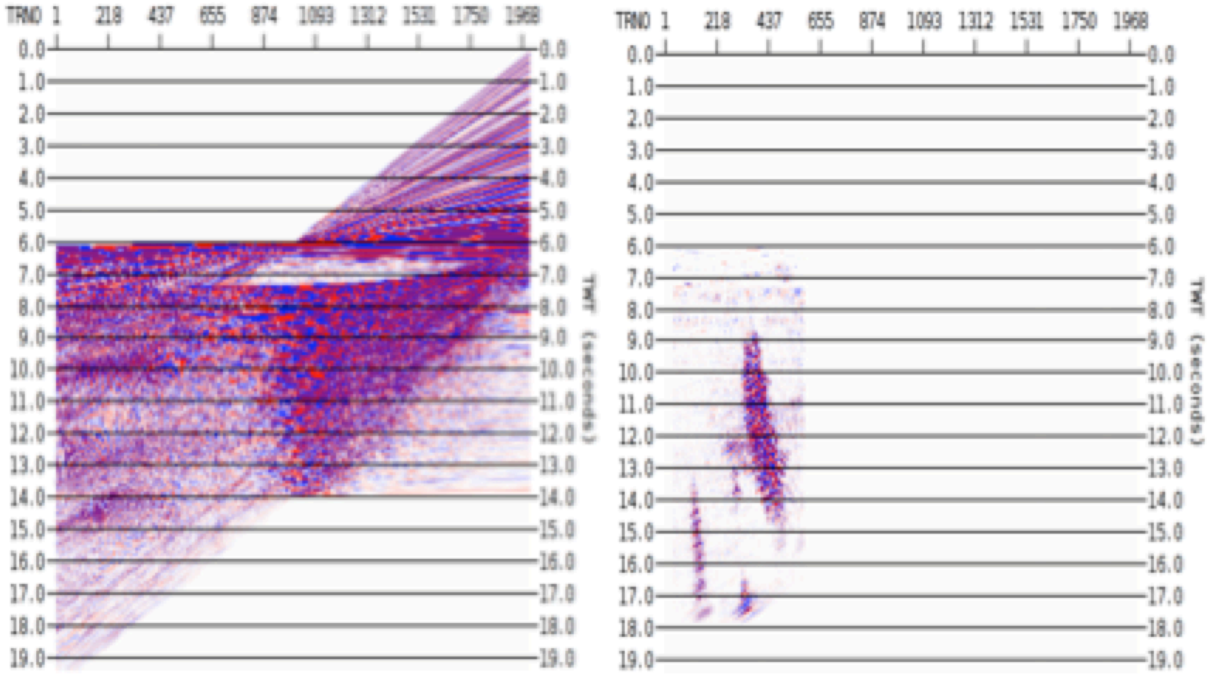

Figure 29: Filtered (τ-p)-gather (left) and removed SI (right).

4. Inverse transformation back to shot gathers

   Finally, we apply an invers (τ-p)-transformation to obtain source gathers in the space-time domain.

The same processing parameters have been already used in section 4.2.3.

Fig. 30 shows the final results obtained for one of the shot points. The overall result is quite good.

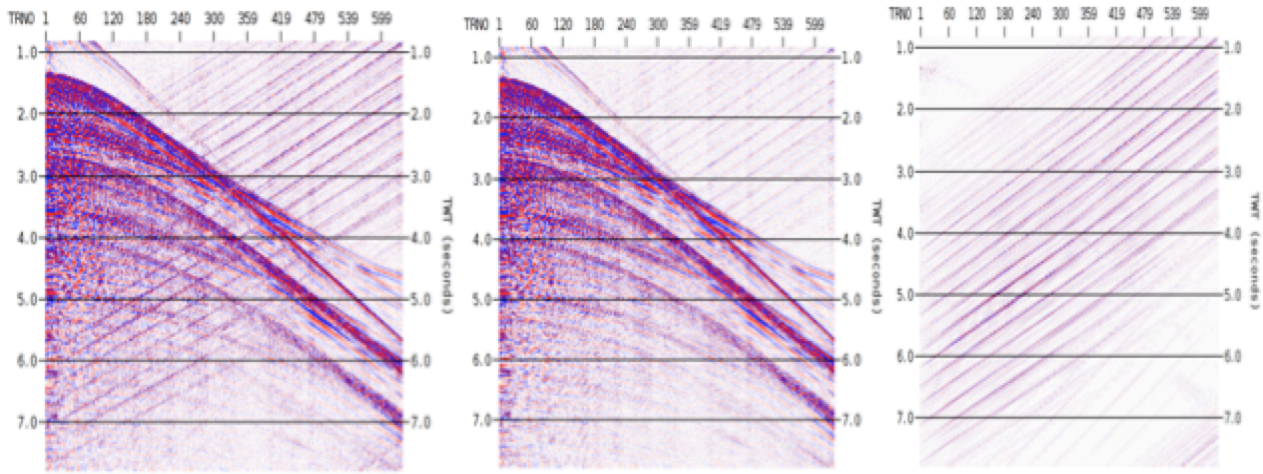

Figure 30: τ-p to common-p method. Original data from shot gather (right), SI filtered data (center) and the difference (left).

At the stage of TFDN filtering, we have two output options. The first one is to choose the filtered version of the original data as output. The second one is to choose the actual SI noise being removed (cf. subchapter 4.1).

In this thesis work we also tested if a better result could be obtained by first outputting the removed noise and then apply an adaptive subtraction process to extract it from the original input data (contaminated with SI).

Parameters used for these two processing strategies are summarized below:

Direct subtraction

Table 10: Direct subtraction parameters.

KEYS	ITRIAL
HEAD	RAW

Adaptive Subtraction

Table 11: Adaptive subtraction parameters.

MODE	SUB
OPUT	DATA
KEYS	ISEQN
ADAP	1, 100, 500, 24
STIM	IWATTIM, 0.9

Parameters in Tables 11 and 12 represent:

- KEYS: used to override the default KEY used for interpolation
- ITRIAL: trial number
- ISEQN: sequential record number
- HEAD: determining which set of trace headers to use on the output data
- RAW: the unprocessed data
- MODE: defines the different types of matching filter
- SUB: a simple subtraction
- OPUT: provides the option to output the estimated noise
- DATA: the result after noise removal
- ADAP: defining the parameters of adaptive matching filter.
- STIM: specifies the start time for the matching process.

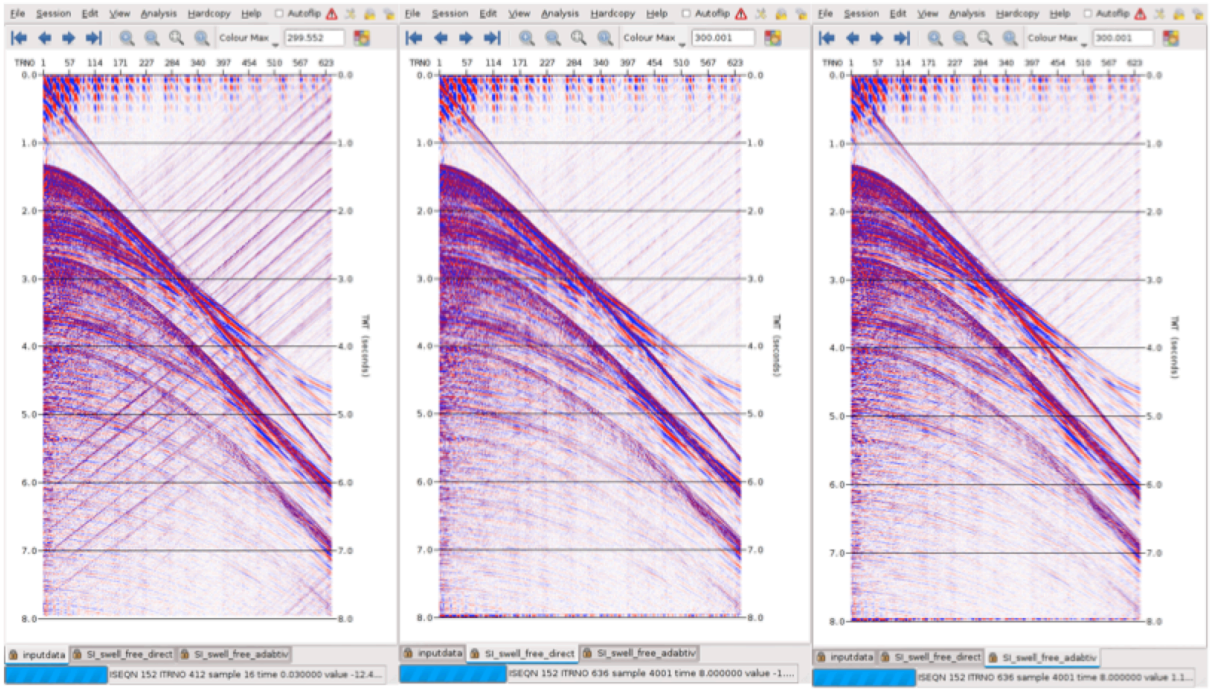

Figure 31: Original shot gather (left), SI removed by direct subtraction (center) and SI removed by an adaptive subtraction (right).

Fig. 31 summarizes the results obtained using the two approaches. In this case, they seemed to perform equally well.

6. GEOLOGICAL AND DATA DESCRIPTION

This chapter discusses briefly the geology of the acquisition area. In addition, the actual data set is reviewed.

6.1 Geological description of the acquisition area

The survey location is in the Faroe-Shetland Basin (FSB), west of Shetlands and northern tip of Scotland. The oceanic beds in this area with volcanic origin are made up of horizontal flows of basalt plateau with some layers of volcanic ash, sandstones, clay and lignite in between (Phil, 2007). Basaltic beds give higher sound wave velocity that can lead to poor subsurface reflectors. The data quality in the acquisition area was good with several strong subsurface reflectors clearly visible. It means that the acquisition area may have other types of rock than basalt. Fig. 32 shows a geological map of Western Europe, with the activity area marked by a blue arrow.

Figure 32: Geological Map of Western Europe (Shepherd, 2002). The acquisition area is marked with a blue arrow.

Huge rift basins exist on the northeast Atlantic margin, which can represent a paleo-propagating rift (Fletcher et al., 2013). The Faroe-Shetland Basin is one of such basins. The crust in the FSB area have experienced thinning and formed an extensional basin. According to Gabrielsen, R. H. (2010), the rifting processes that takes place in such a basin consist of:

- Pre-rift: shown in Fig. 33 (A), easy fracturing and expansion of the lithosphere caused by a magma chamber from the mantle.
- Syn-rift: shown in Fig. 33 (B), the crust and upper mantle lithosphere becomes thinned and promoted by extensional faulting, the basin floor will subside quickly. This implies that deeply seated warm rocks are transferred upward in the lithosphere so that the isotherms and thermal gradient in the thinned area will increase.
- Post-rift: shown in Fig. 33 (C), the basin is cooled and will continue to subside due to a combination of thermal contraction, sediment compaction and sediment loading.

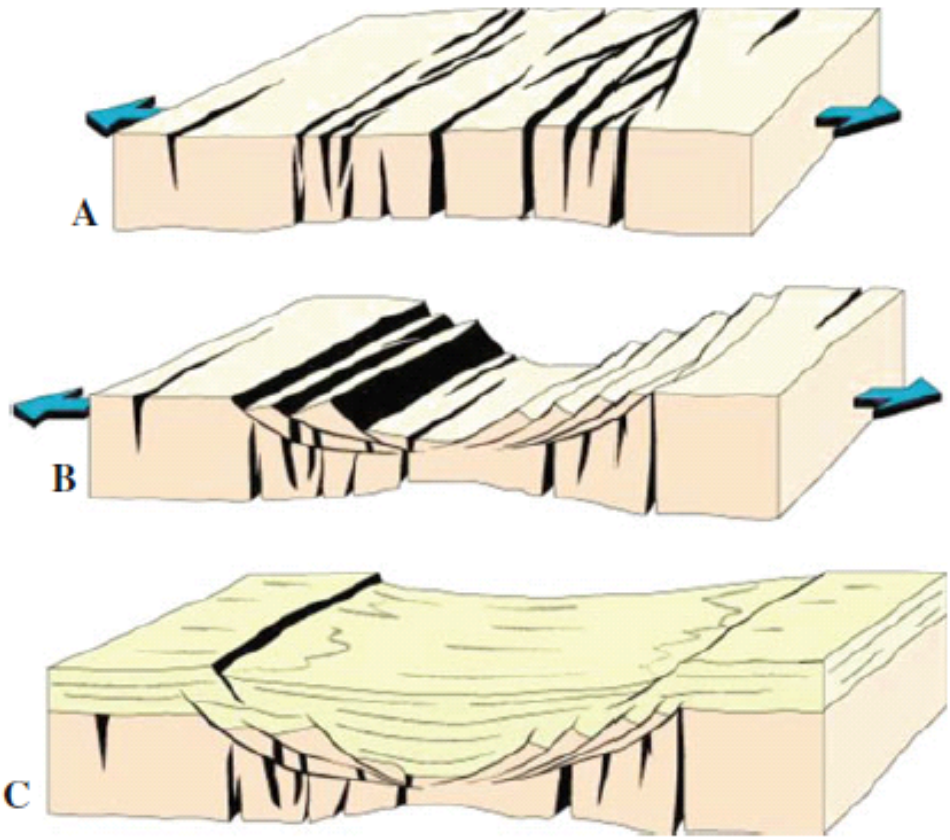

Figure 33: Showing three major stages in the development of extensional basins. The pre-rift (A), the syn-rift (B) and the post-rift (C) (Gabrielsen, 2010).

Fletcher et al. (2013) have reported that the main rifting event in FSB started in Mesozoic after intracontinental rifting. The Mesozoic syn-rift sediments were followed by post-rift Cenozoic sediments resulting in subsidence and compaction of sediments. In late Paleocene, an uplift and a rapid subsequent subsidence has been reported which has interrupted the post-rift subsidence in the basin. The uplift occurs at the same time as the continental break up between Europe and North America. At this time the center of FSB has accommodated 1.9 km of sediments after the Paleocene age.

Fig. 34 shows the regional composite seismic profiles across the FSB. Interpretation of these seismic surveys shows the present day architecture of the region.

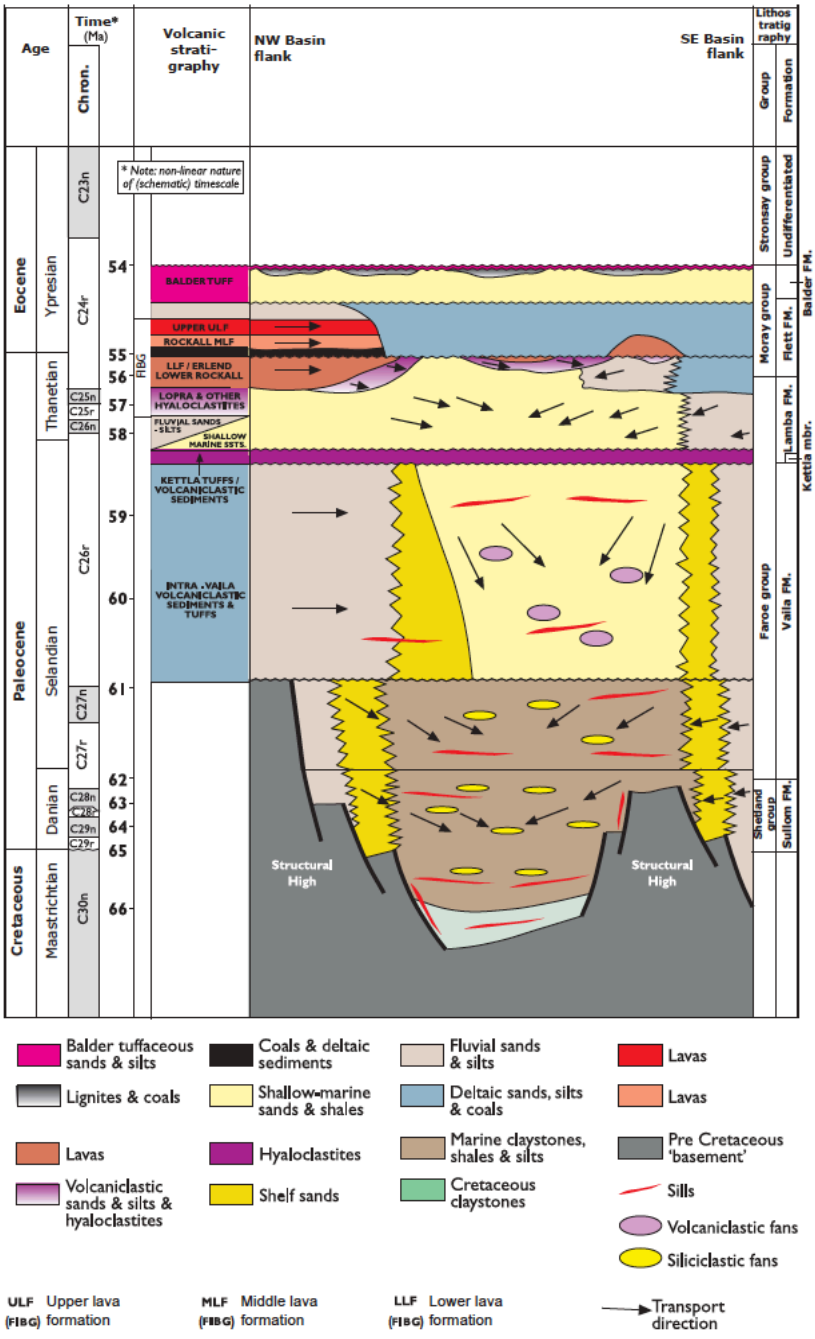

Figure 34: Regional composite seismic profiles across the FSB (Fletcher et al., 2013).

Also, a stratigraphic column associated with this region is shown in Fig. 35.

As indicated in this column, the volcanic basalt has covered the region in the Paleocene age due to continental break up. Afterwards, the volcanic basalt is covered by volcanic ash and volcaniclastic sediments.

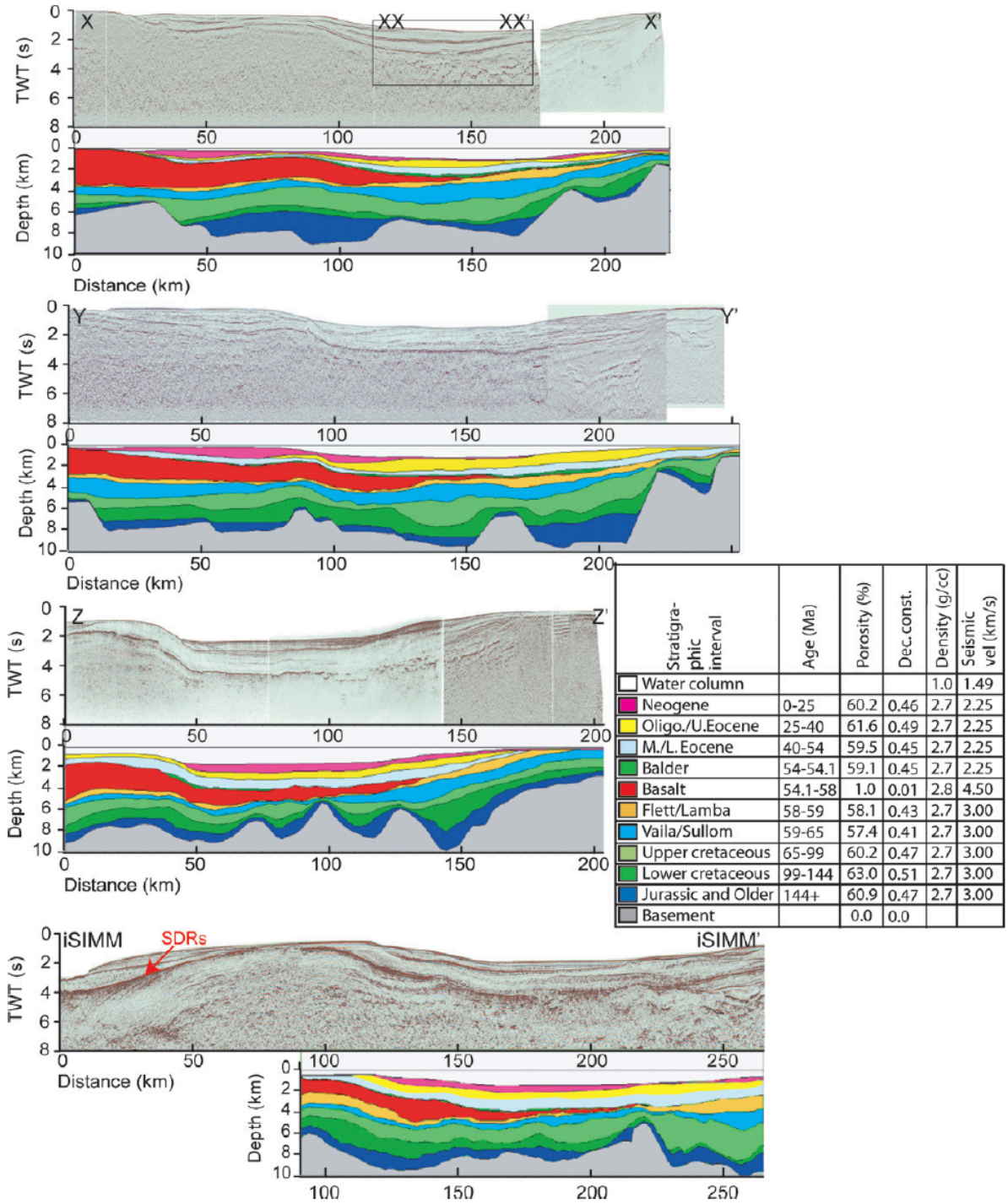

Stratigraphic interval	Age (Ma)	Porosity (%)	Dec. const.	Density (g/cc)	Seismic vel (km/s)
Water column				1.0	1.49
Neogene	0-25	60.2	0.46	2.7	2.25
Oligo./U.Eocene	25-40	61.6	0.49	2.7	2.25
M./L. Eocene	40-54	59.5	0.45	2.7	2.25
Balder	54-54.1	59.1	0.45	2.7	2.25
Basalt	54.1-58	1.0	0.01	2.8	4.50
Flett/Lamba	58-59	58.1	0.43	2.7	3.00
Vaila/Sullom	59-65	57.4	0.41	2.7	3.00
Upper cretaceous	65-99	60.2	0.47	2.7	3.00
Lower cretaceous	99-144	63.0	0.51	2.7	3.00
Jurassic and Older	144+	60.9	0.47	2.7	3.00
Basement		0.0	0.0		

Figure 35: Stratigraphic column associated with this region (Fletcher et al., 2013).

However, we do not observe basalt in the data, which might indicate that we have good data quality.

6.2 Data description

The data used in this thesis was acquired in the Faroese water, west of Shetlands and the northern tip of Scotland in 2013, see Fig. 36.

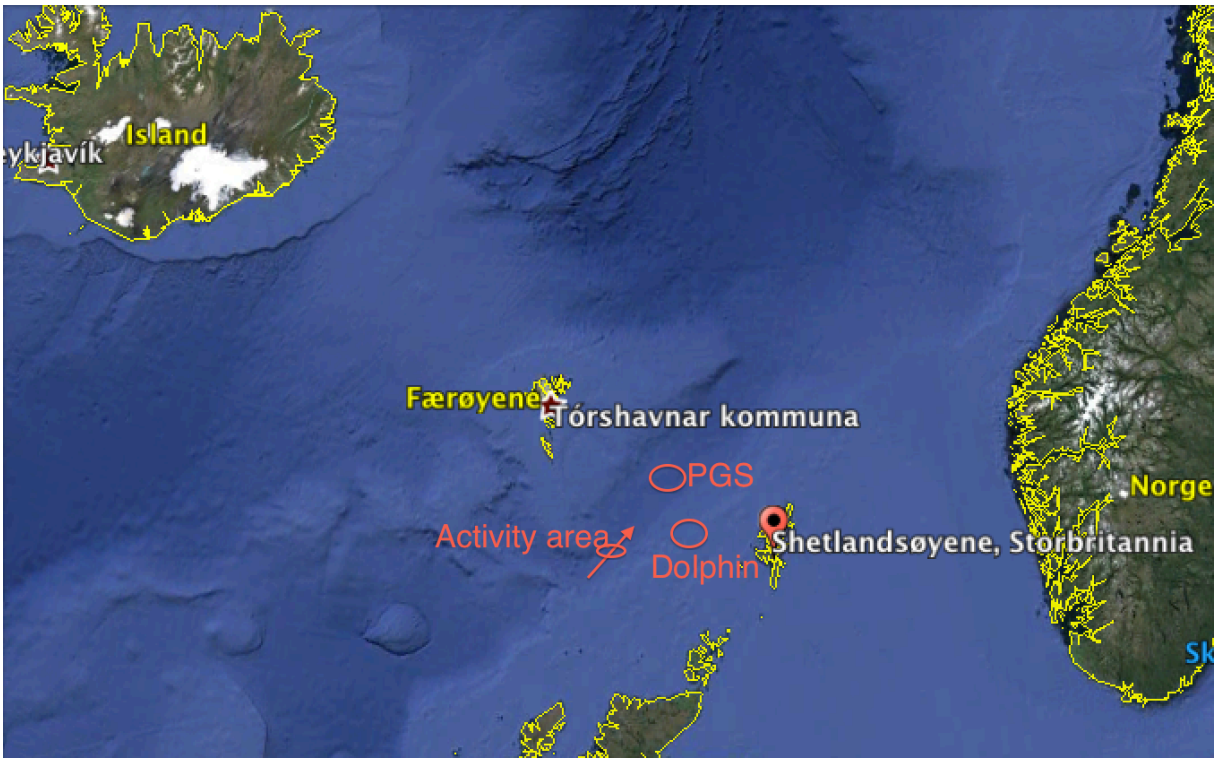

Figure 36: Activity area and direction (red pile) of survey. Activities from other vessels of PGS and Dolphin (red circles) seen during the survey.

The Faroe Islands are located approximately 600 km west of Bergen and consists of 18 islands of volcanic origin.

During the acquisition the weather was fair. However, at times some light swell noise was observed.

Two sources of seismic interference were seen during the survey. One of them was due to the PGS Ramform Explorer that was located 130 km (closest point) to the north of our test lines. The second was Dolphin Sanco Swift that was located around 100 km to the northeast of our test lines.

Details about the streamers in use as well as the source array can be found in Tables 13 and 14.

Streamers

Table 12: Streamer parameters

Number of Channel	638(p) and 96(v_z and v_y)
Streamer active length	7950m (P), 1200m Multicomponent data
Streamer type	Sentinel seal 2Hz, 6dB/oct. & Sentinel MS
Trace interval:	12.5m
Seismic offset:	150m
Streamer depth:	12m / Broadseis 12-50m
Number of birds per streamer	DigiBirds: every 750m along streamer, 150m for head and tail. Nautilus: every 300malong streamer 150m for head and tail.
Number of acoustics per streamer	Nautilus NSN every 300m (150m in the front)

EDV Energy source

Table 13: EDV Energy source parameters.

Source type:	Sercel GGII
Number of arrays:	1
Number of sub-arrays per array:	3
Source array depth:	4.5
Nominal air pressure:	2000psi
Volume:	4600cuin

As can be seen from Table12, also a short multi-component streamer was used as part of the survey. Multicomponent seismic arrays consist of three components (3C). A hydrophone which measure pressure (P) and two sensors where one of them measures the velocity in Y-direction (V_y) and the other measures the velocity in the Z-direction (V_z). Multi-component seismic recordings (measurement with vertical- and horizontal-component) captures the seismic wave field more completely than conventional P-wave techniques and allows for determining the direction of wave propagation.

This multi-component data set was the focus in this thesis work, consisting of 400 continuously recorded shot gathers.

Fig. 37 shows one shot recorded for the P-data before and after application of a low cut filter of 3Hz.

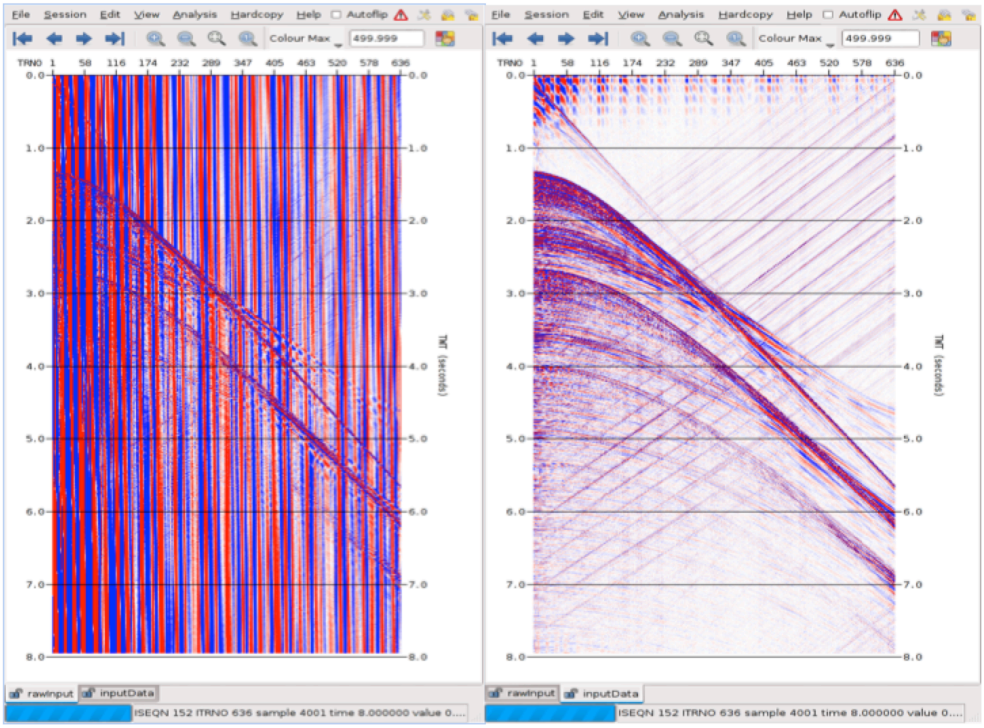

Figure 37: Raw p-data (left) and after low cut filter (right).

After removing the swell noise from the raw data, the quality of the P-component data looks adequate. The SI noise in this data can be clearly seen as inclined lines downwards to the left.

Fig. 38 shows a shot record of the V_y-component before and after low cut filtering to 30 Hz. This figure evidently shows that the Y-component does not give reliable signals and is heavily noise contaminated. Therefore, we cannot directly use data acquired by this component for imaging.

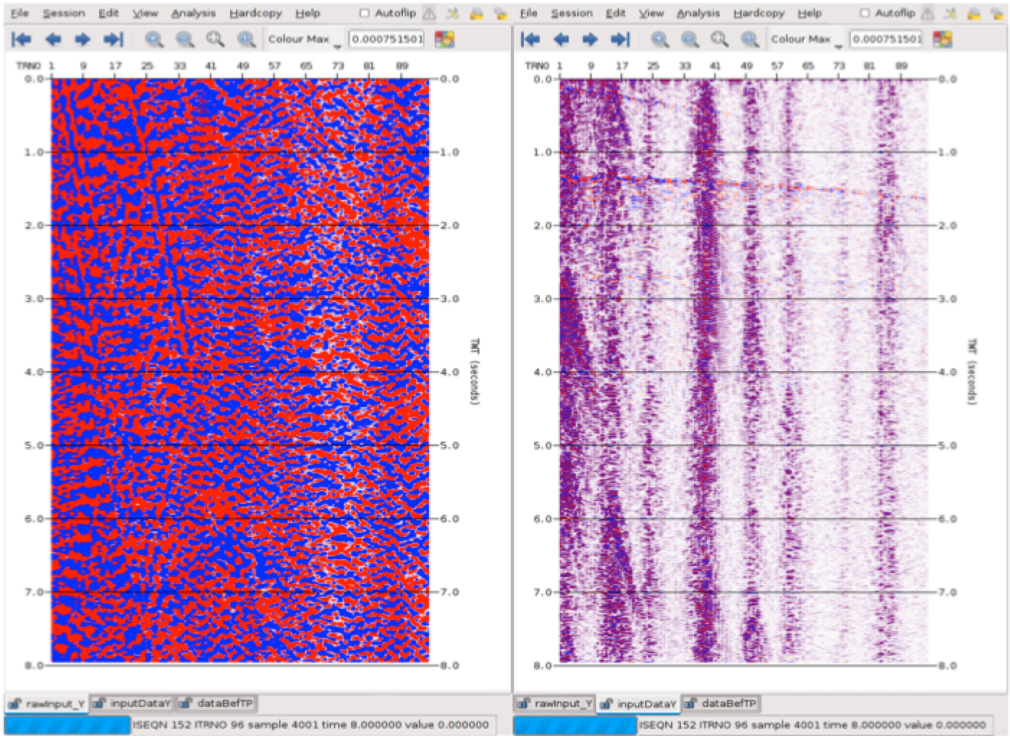

Figure 38: V_y-values of raw data (left) and after low cut filter (right).

Finally, Fig. 39 shows a shot record of the V_z-component before and after low cut filtering to 25Hz.

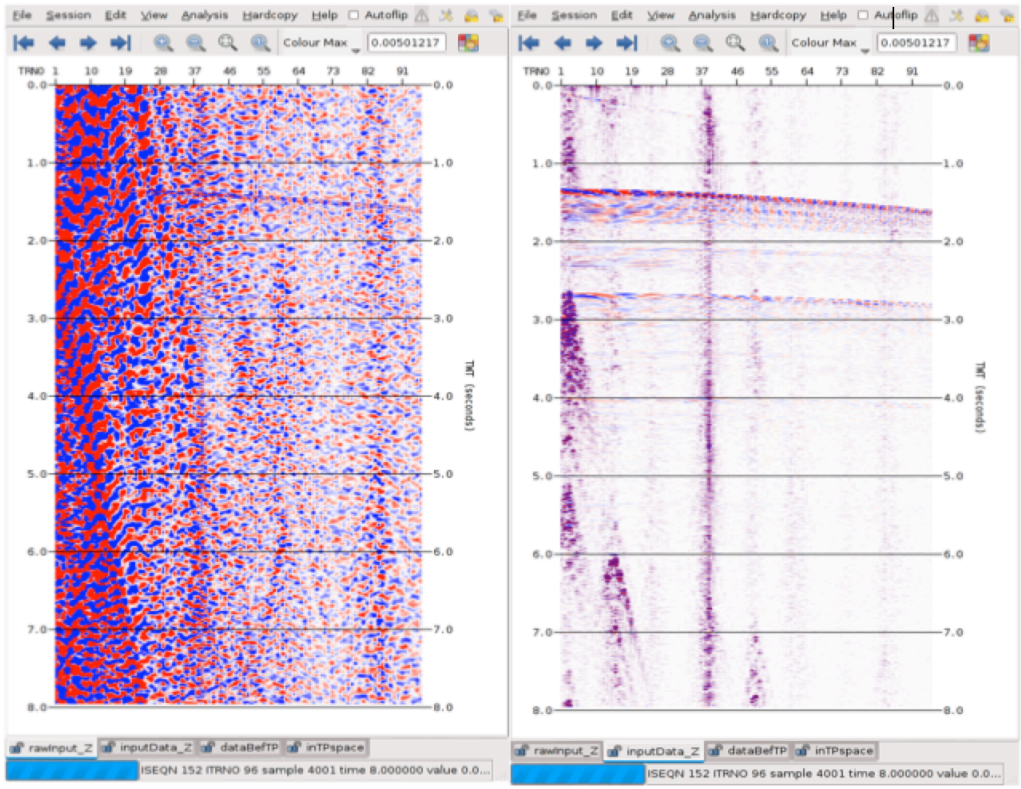

Figure 39: V_z-values of raw data (left) and the result after low cut filter (right).

Unlike the V_y-component, some parts of the data can now be recognized after low-cut filtering. The V_z-component should carry similar information as the pressure recording, but on comparison with Fig. 37 much information are not easily recovered in Fig. 39.

Since both the V_z- and V_y-components were heavily contaminated by streamer noise, the use of them in this thesis was made difficult. Thus, the majority of results were therefore obtained using P-data only.

7. RESULTS

In this chapter the complete processing of the field data (P-component) is being presented including stacking and post-stack migration.

Two identical processing lines were followed when creating the stack and post-stack migration but with different input: in one case we used the original data including SI and in the other case data after SI removal.

7.1 Finding dips of real data

Before starting the more comprehensive processing, a MATLAB code was run to identify the dip range of the SI noise. This makes it possible to run the (τ-p)-transformation in a more efficient way. Fig. 40 shows a flow of the MATLAB calculations.

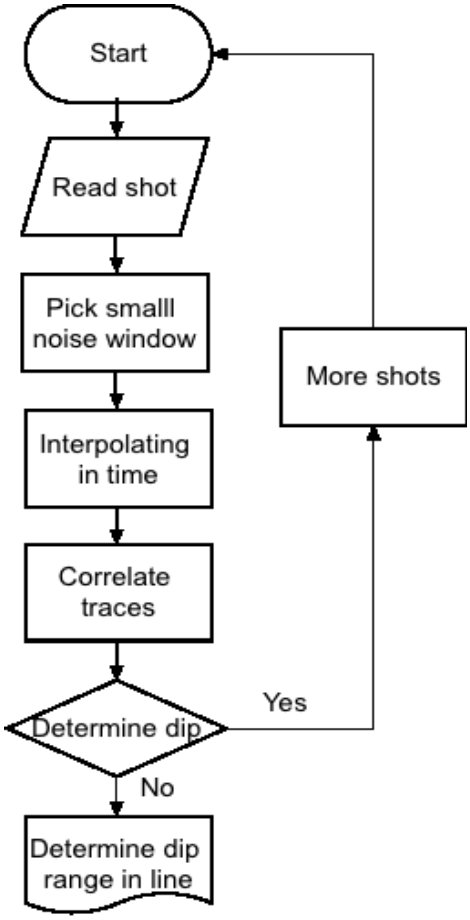

Figure 40: Flow of MATLAB work.

A small noise window in the upper right corner before the direct wave arrival was chosen, as illustrated in Fig. 41. In this way we can determine the dip of the SI noise.

To increase time resolution, the values between the data points were interpolated. A fairly optimum interpolation factor for this purpose was determined to be 30. Interpolation factors greater than 30 do not introduce significant change in the output result and just increase the CPU time.

A threshold value of 0.9 for cross correlation was used for the dip calculations. Cross-correlation measures the similarity of two waveforms as a function of time lag applied to one of them (Kearey, 2002). A waveform is sliding past the other waveform and for each time shift, or time lag, we are summing the cross multiplication products to derive the cross-correlation as a function of lag value. Assuming two digital waveforms of finite length, x_i and y_i (i = 1, 2… n), the cross-correlation function is given by (Kearey, 2002):

$$\emptyset_{xy}(\tau) = \sum_{i=1}^{n-\tau} x_{i+\tau}\, y_i (-m < \tau < +m) \qquad (7.2)$$

where τ is the time lag and m is known as the maximum value of the function.

Correlation is normally used to include a standardizing factor in such way that correlation has values between -1 and +1, where 1 means similar, 0 means non-similar and -1 means opposite.

Besides the P-data, the velocity sensor data V_y and V_z were also tested for dip estimation (this time with a much lower threshold of 0.2). However, due to the noise no reliable estimates could be obtained.

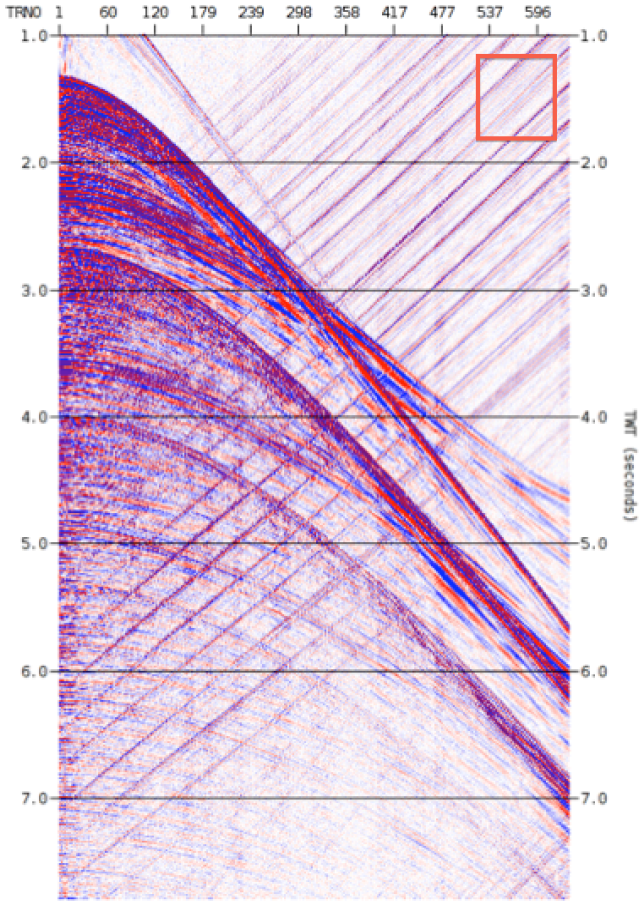

Figure 41: Chosen noise window shown in red used in MATLAB program.

7.2 The first processing flow - including SI-removal

From the dip estimation study a dip range between -2000 to -4000 were obtained for this line. The values are negative because of the dip direction. During processing the same τ-p to common-p technique as discussed in chapter 5 was employed but conditioned with the dip range found from running the MATLAB code. The filtered shot records were then input to a standard processing flow to NMO correction, stacking and post-stack migration. The processing flow is shown in Fig. 42.

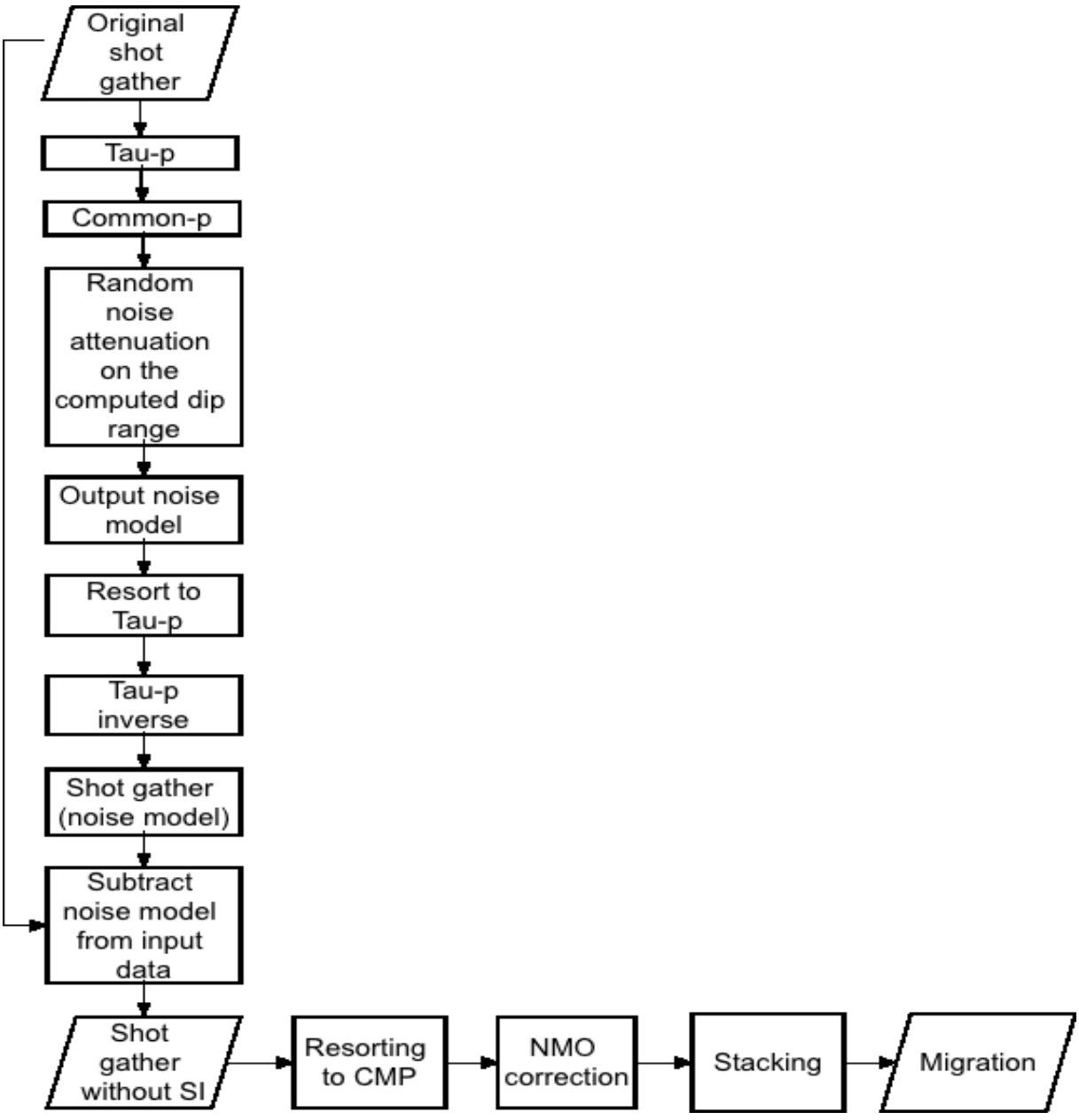

Figure 42: Processing flow.

In the following, the main results from this processing flow are presented. In Fig. 43 the result before and after filtering is shown in the (τ-p)-domain. The actual removed data is shown in the same figure.

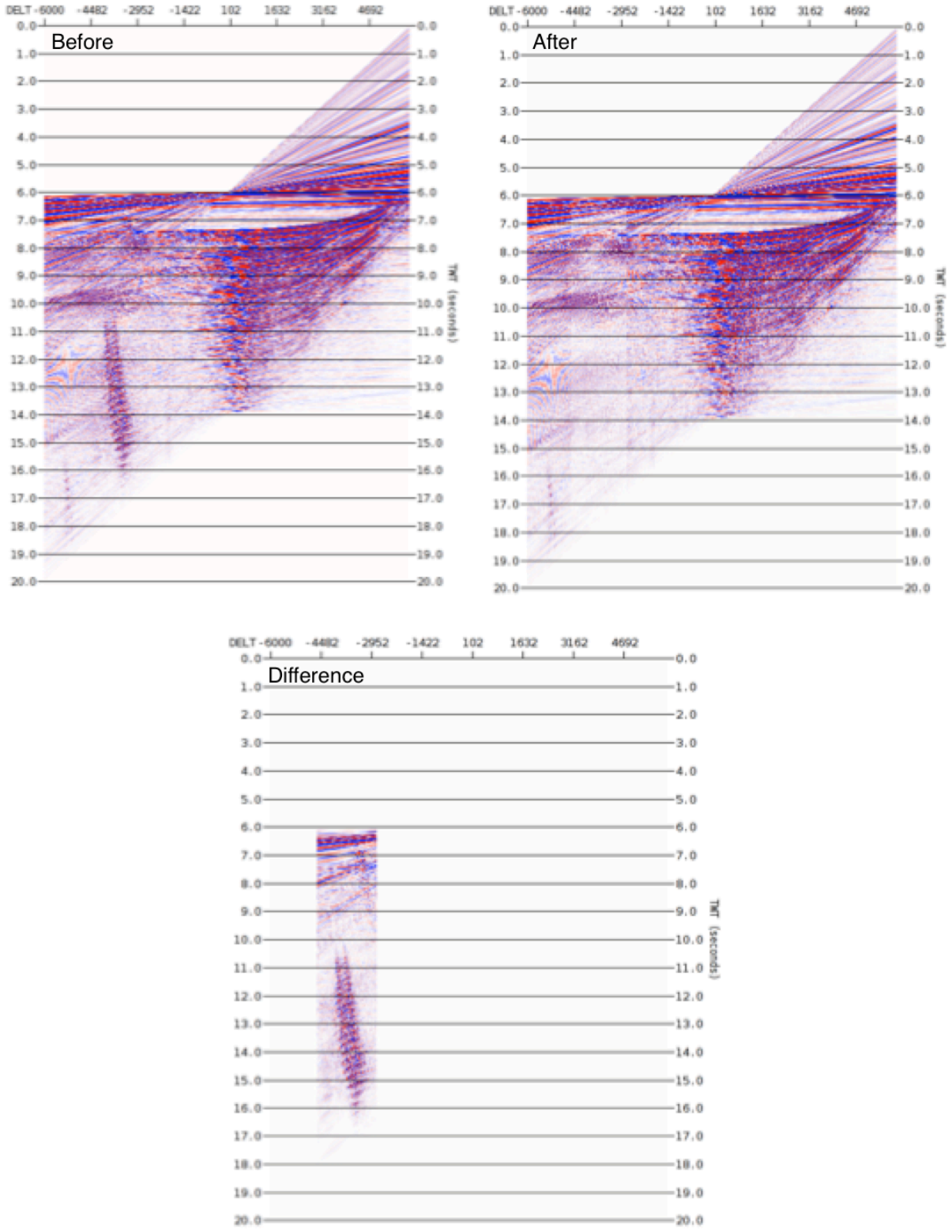

Figure 43: (τ-p)-gather data with SI (upper left), after filtering (upper right) and the difference (lower).

In Fig. 44 the same type of result is shown, but now with data sorted in common-*p* gather.

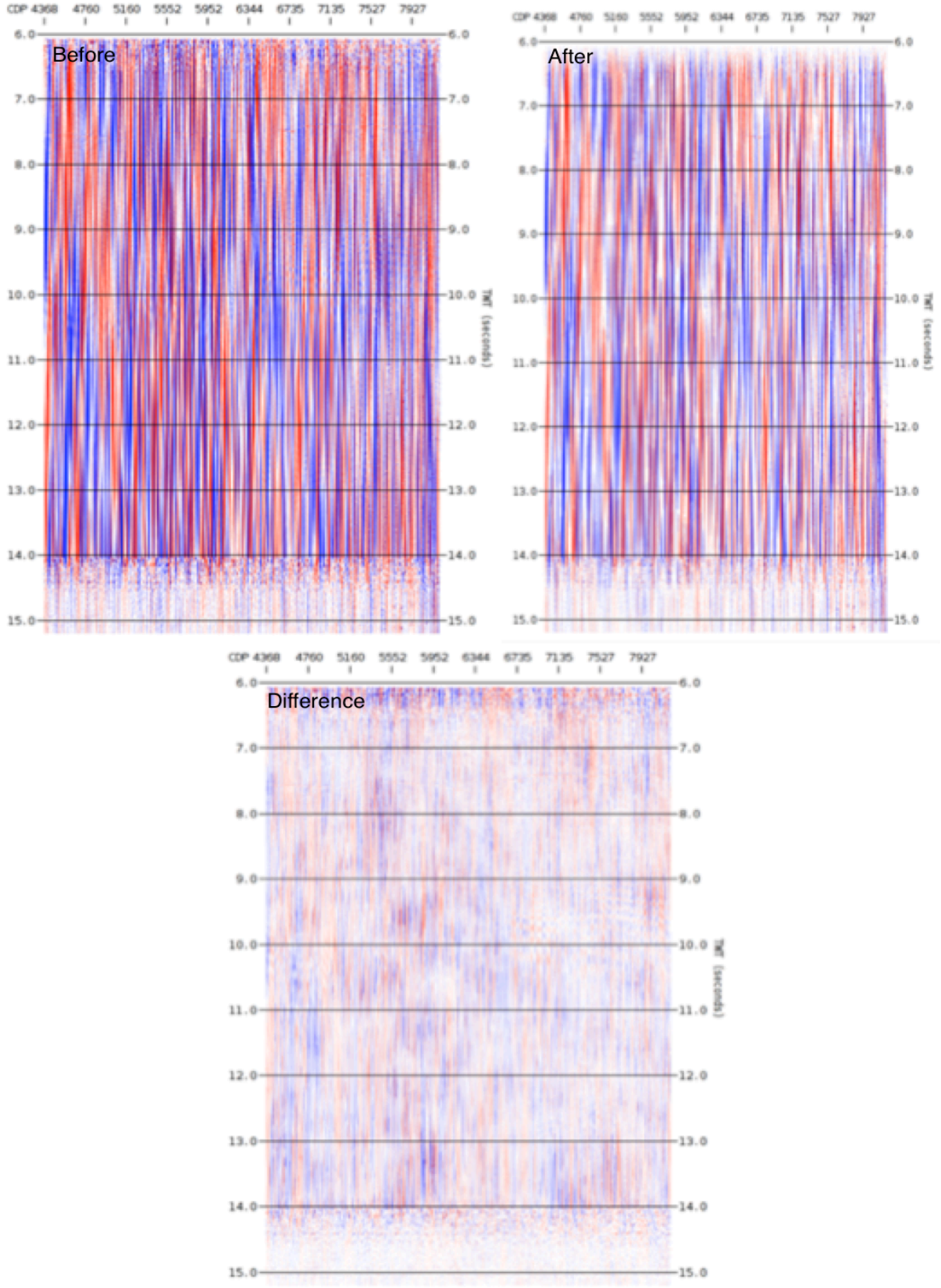

Figure 44: Common-p gather. Data with SI (upper left), filtered data (upper right) and difference (lower).

After inverse (τ-p)-transformation we can observe the same results but now in space-time (shot record), see Fig. 45.

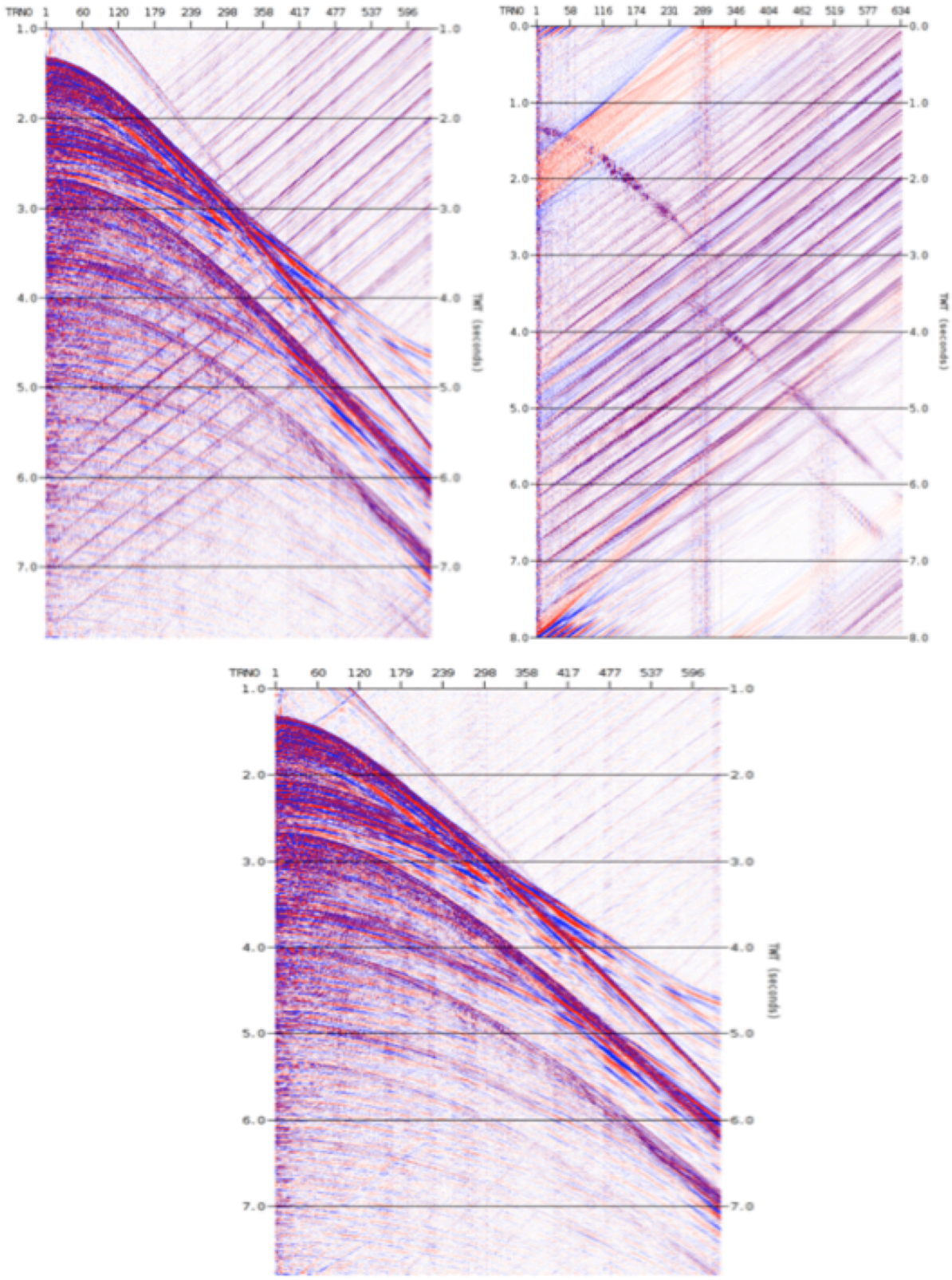

Figure 45: Original shot gather (upper left) noise model (upper right), which is output from the τ-p to common-p job, and the difference (lower), which is the shot gather after SI removal.

The results after stacking are shown in Fig. 46. By considering a selected area (see rectangle), it can bee seen from the difference stack that the SI noise have been removed efficiently. However, it has to be said that the noise (the amplitudes in the difference plot) is very low as expected due to the stacking process.

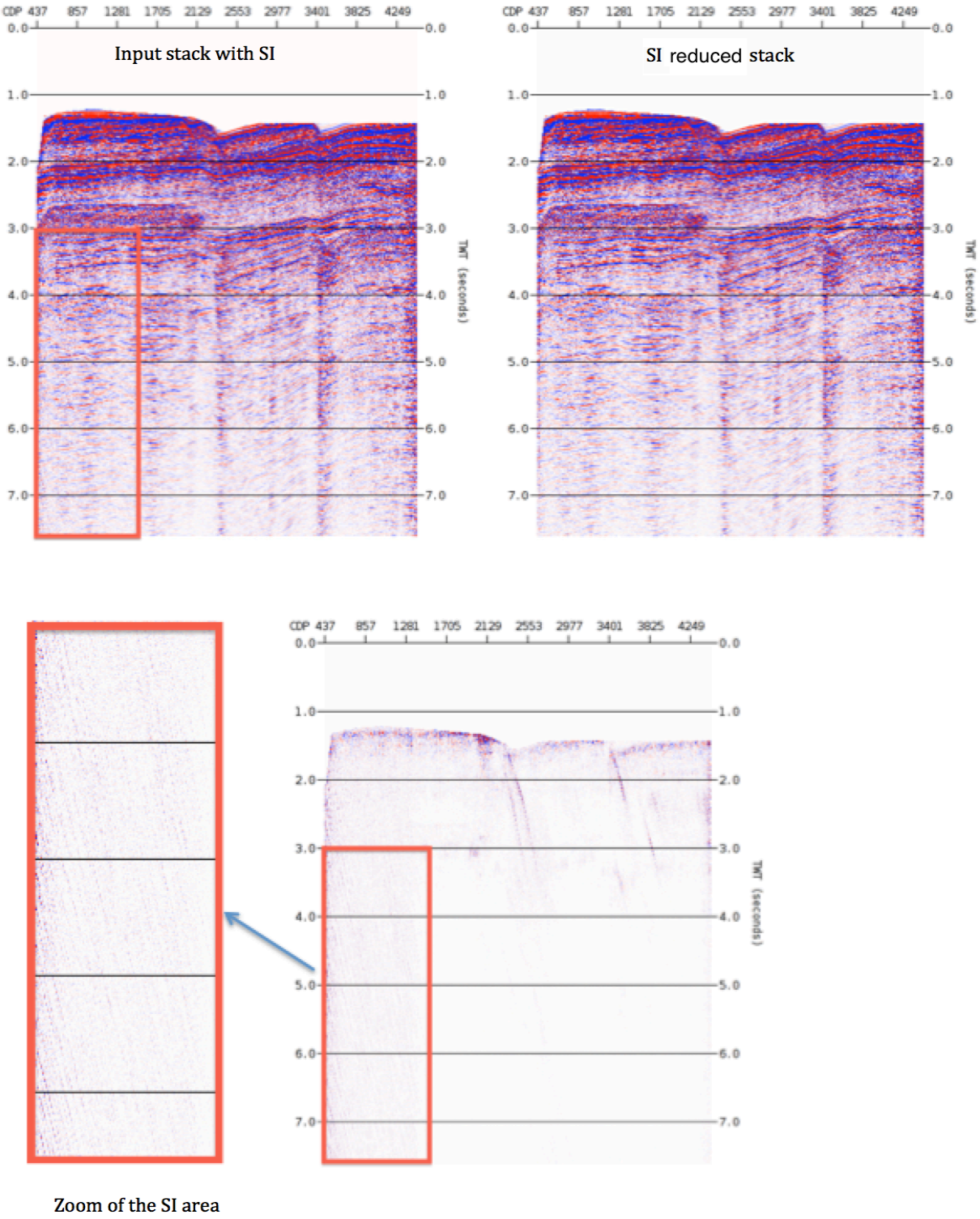

Figure 46: Input stack (left) with SI. SI is visible inside red rectangle. Output stack (right) with SI being filtered and the difference (lower).

Finally, the result after migration is shown in Fig. 47, with input being the stacked section with SI-filtering.

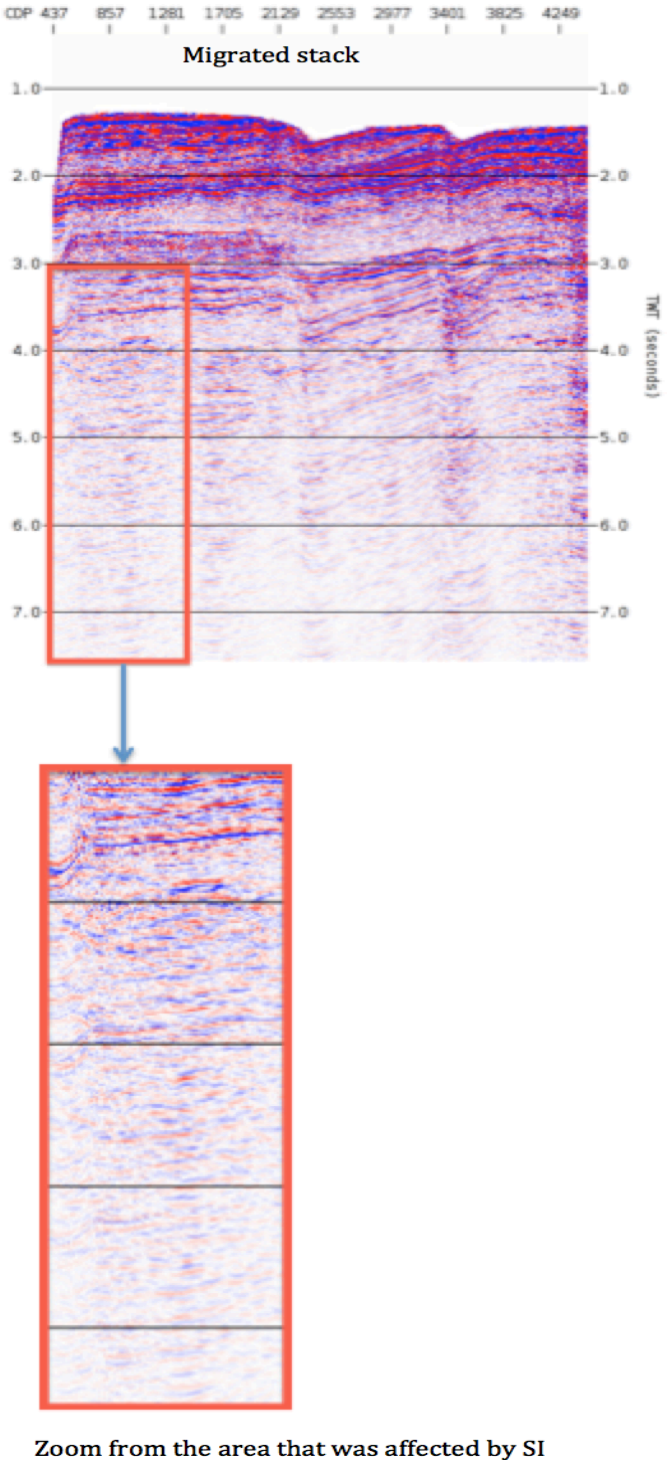

Figure 47: Migrated section with zoom area.

Considering the same selected area as in Fig. 46, no traces of SI noise can be found after migration.

7.3 The second processing flow – original data

In the second flow the stacked and the migrated sections will be generated directly from the original data without SI attenuation. The processing flow can now be summarized as in Fig. 48.

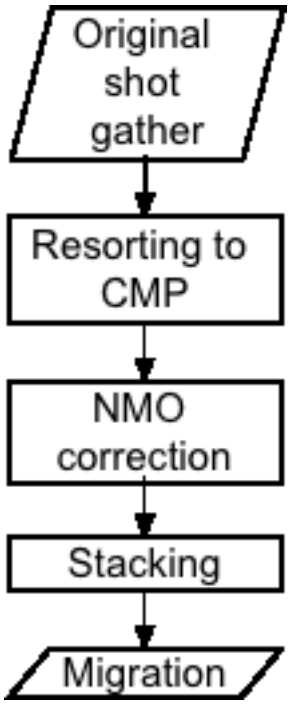

Figure 48: Second processing flow.

Fig. 49 summarized the results obtained, with the same zoomed area selected.

In the next subsection, we discuss the differences between the two processing flows.

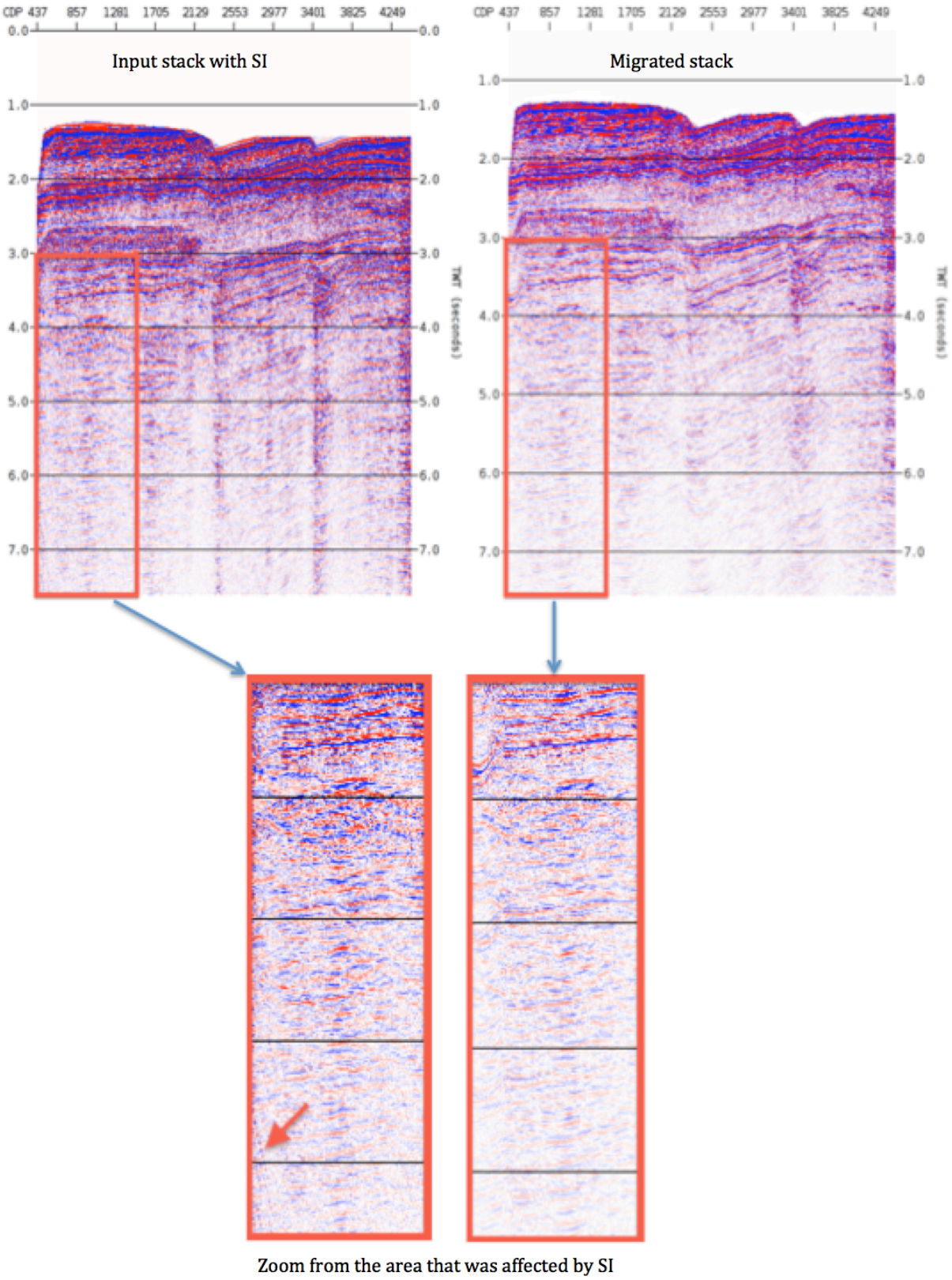

Figure 49: Stacked section with SI (left) and the corresponding migrated section (right).

7.4 Comparison between processing flows 1 and 2

The main results obtained using the two processing flows are summarized in Fig. 50.

The appendix presents the flowchart of comparison between processing flows 1 and 2.

The main observation is that small differences exist post-stack (both in case of stack and migrated section). After migration has been applied, the differences are negligible (see Fig. 51).

This is not a surprise, since migration is a technique tailored for enhancement of coherent events in combination with efficient denoising.

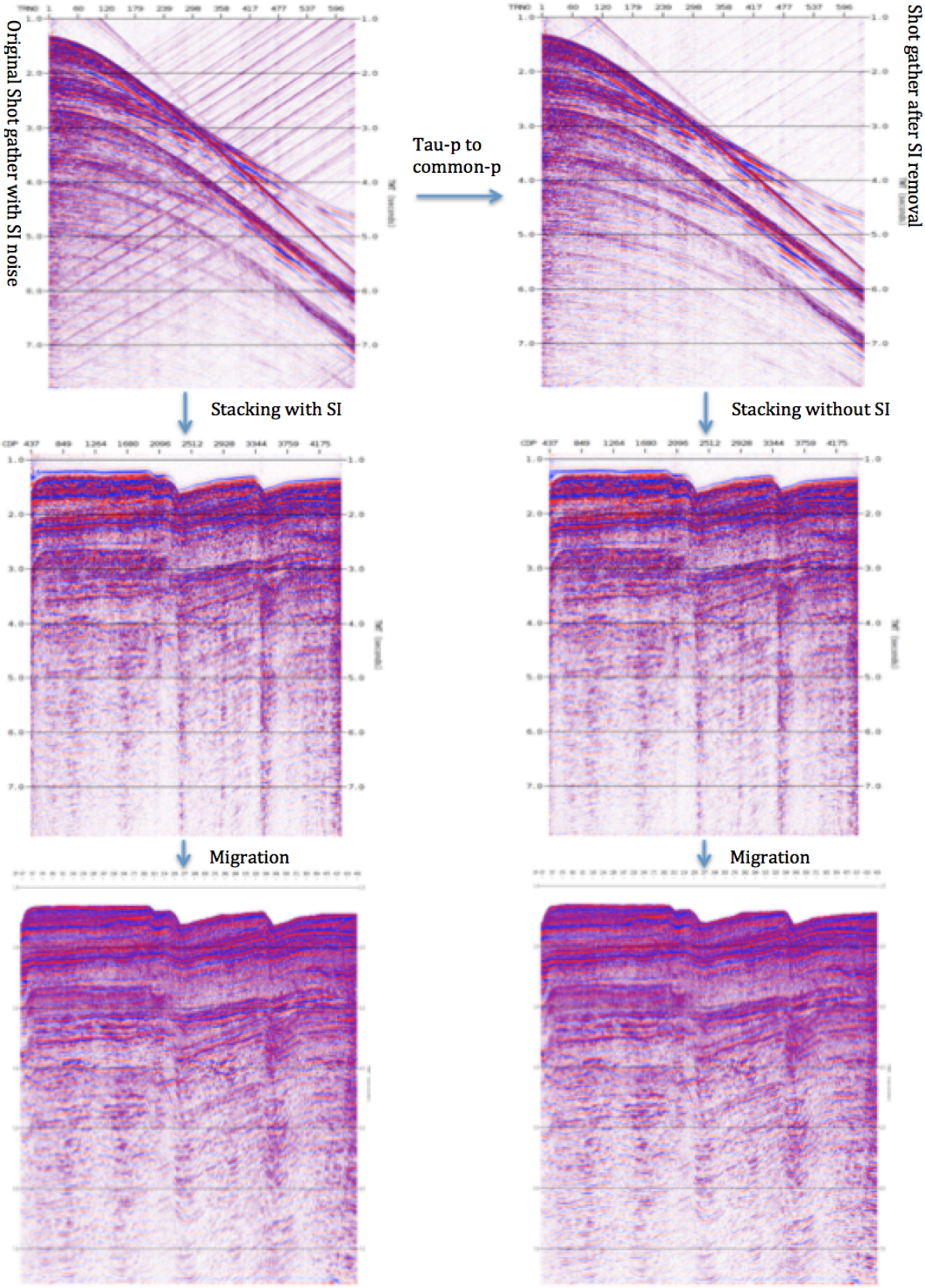

Figure 50: Complete processing flows 1 and 2. Original shot gather (upper left), SI filtered shot gather (upper right), stacked section with SI (center to the left), stacked section without SI (center to the right), migrated sections (lower left and right).

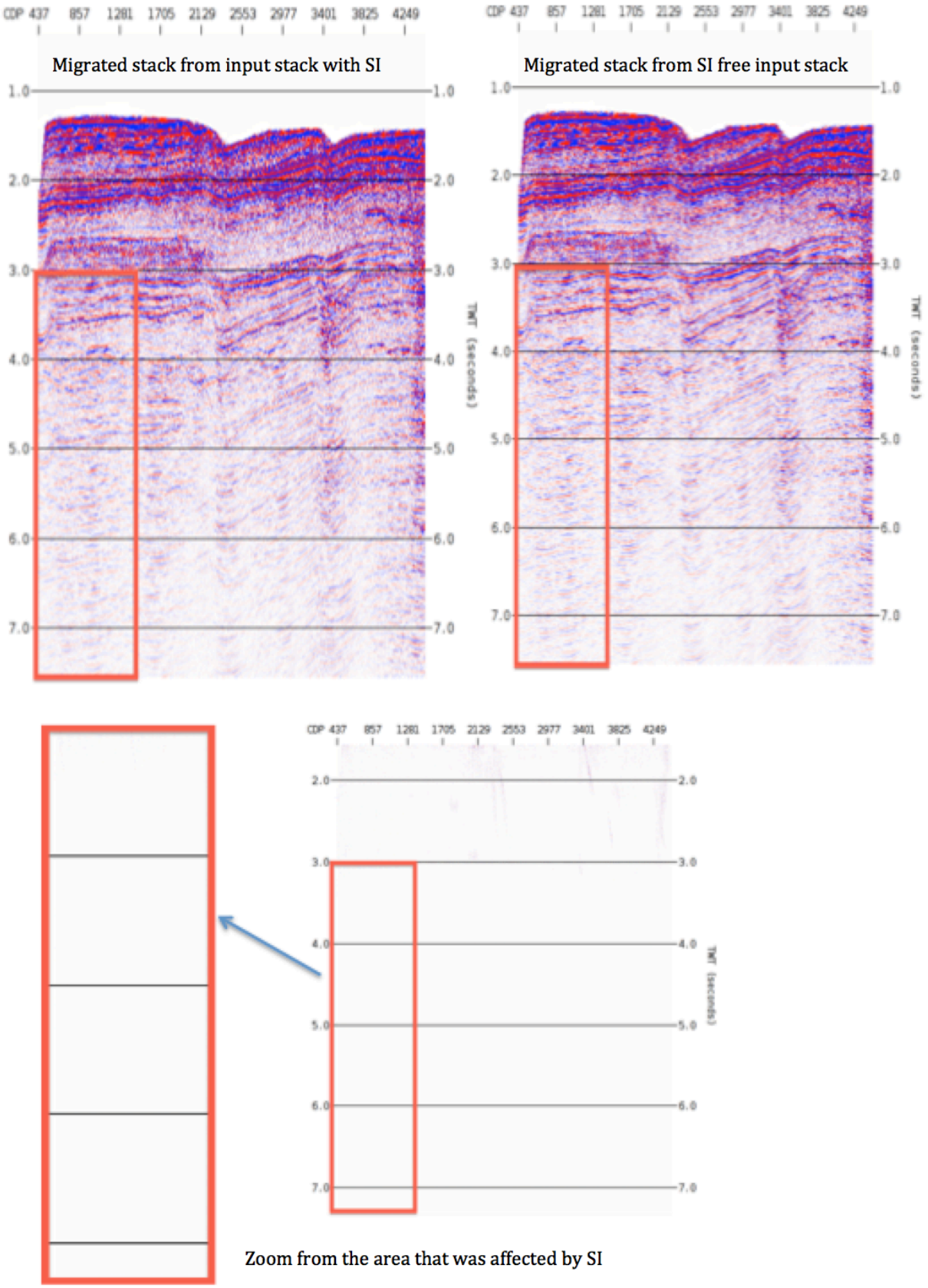

Figure 51: Migrated sections from both processing flows (upper left and right) and the residual section (lower).

8. DISCUSSION OF MULTI-COMPONENT DATA

The original task of this thesis was to use the full recording from a multi-component streamer to characterize and identify SI noise followed by efficient removal. However, the two velocity sensors V_y and V_z were found to be not very useful. The reason is that they are very sensitive to streamer born noise such as transversal vibration noise (Teigen et al., 2012), see illustration in Fig. 52. Such noise will be almost perpendicular to the direction of the propagating wave in the column. Thus the particles do not move along with the wave, but oscillate up and down around their equilibrium position as the waves pass by.

In case of the P-recording, the situation is very different since hydrophones can be designed to be rather insensitive to vibration. This also made it possible to use P-data to characterize the SI-noise, and such data could also be efficiently corrected for SI as demonstrated in chapter 7.

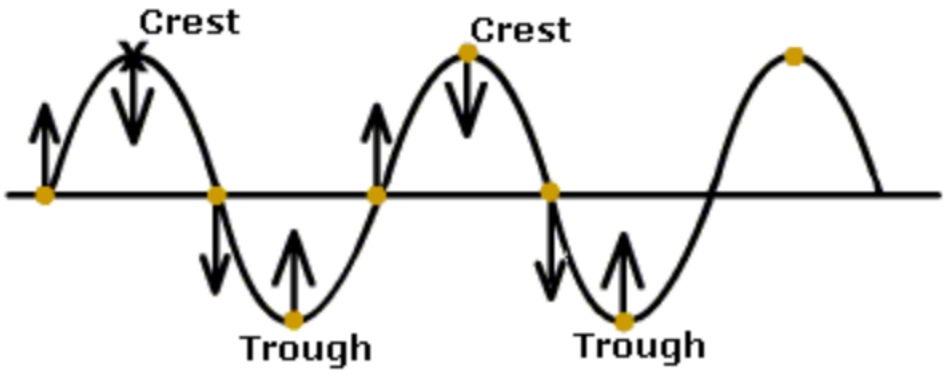

Figure 52: Transverse vibrational movement (www.physics.tutorvista.com).

To further support the main findings, Figs. 53-55 show how the three different components can estimate the directions of the SI noise. As can be seen, the P-data performance is way beyond the two others.

The data used in these figures is from the small noise window before the direct wave arrival was chosen, as illustrated in Fig. 41. In this way we do not have reflection data but pure SI noise.

Subset of P-data.

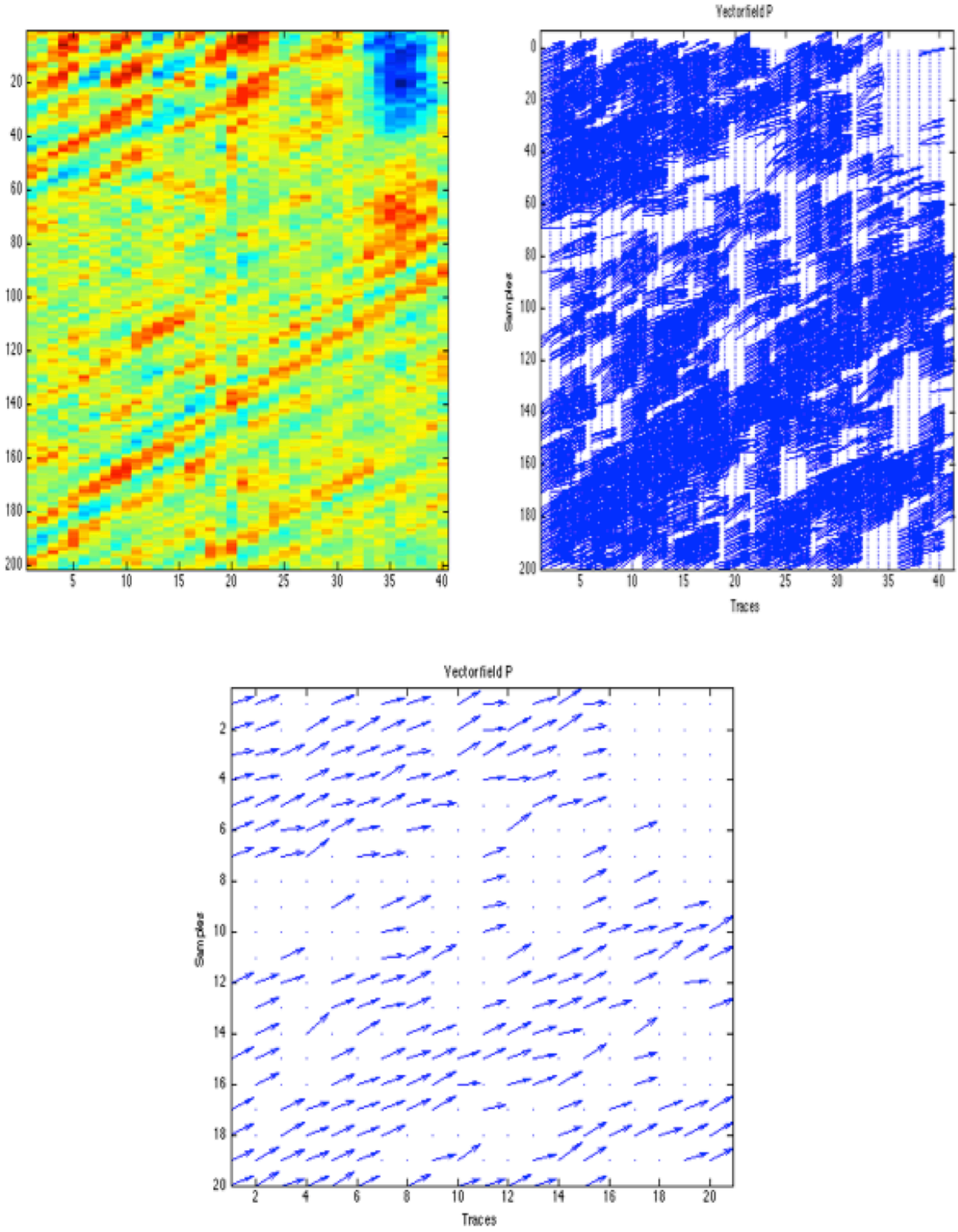

Figure 53: The P- vector field (upper) and the sub-sampled P- vector field (lower). The arrows represent the directions of SI. The dots represent areas where it is not possible to recognize the direction of SI.

Subset of V_y-data.

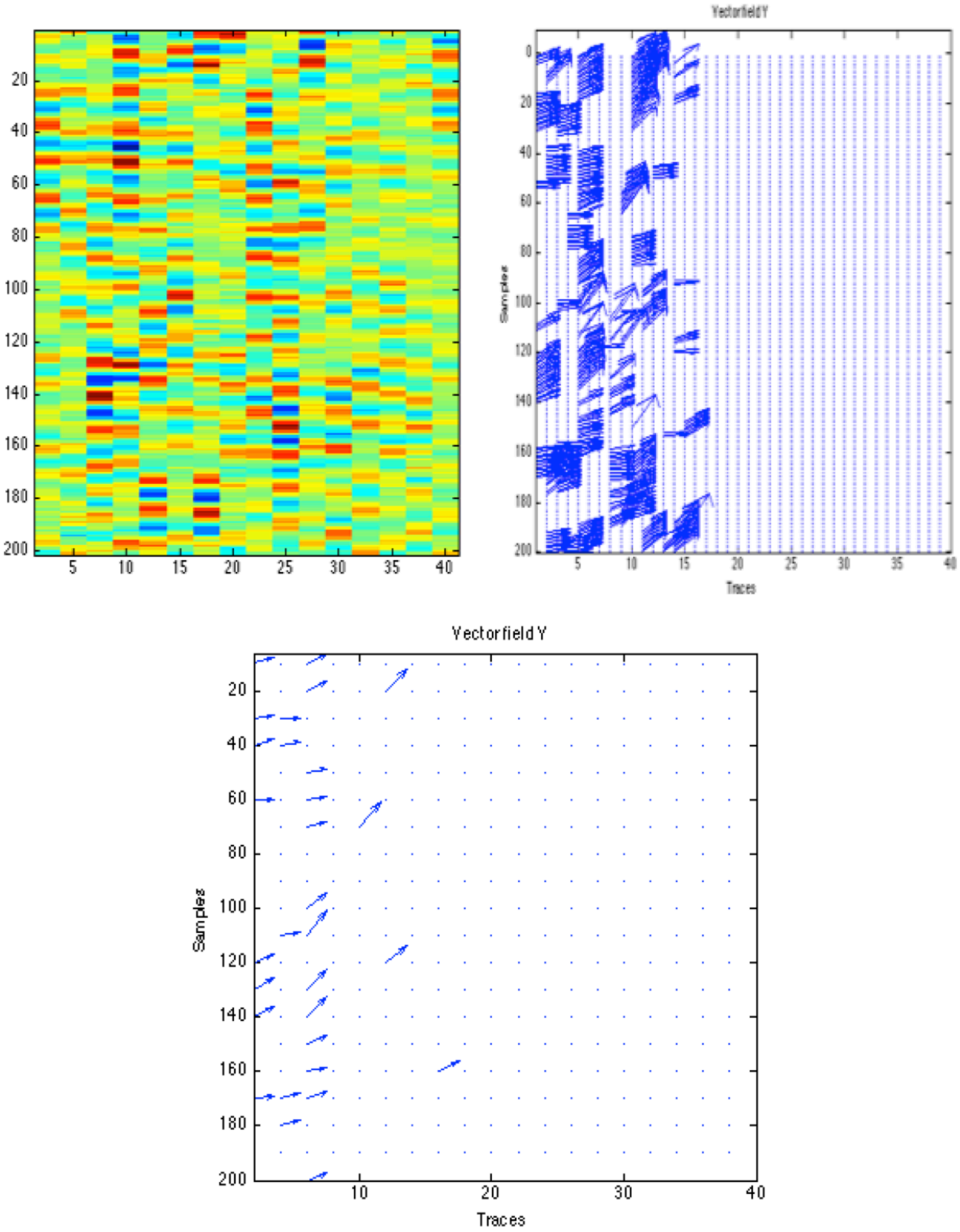

Figure 54: The Y-vector field (upper) and the sub-sampled Y- vector field (lower). The arrows represent the directions of SI. The dots represent areas where it is not possible to recognize the direction of SI.

Subset of V_z-data.

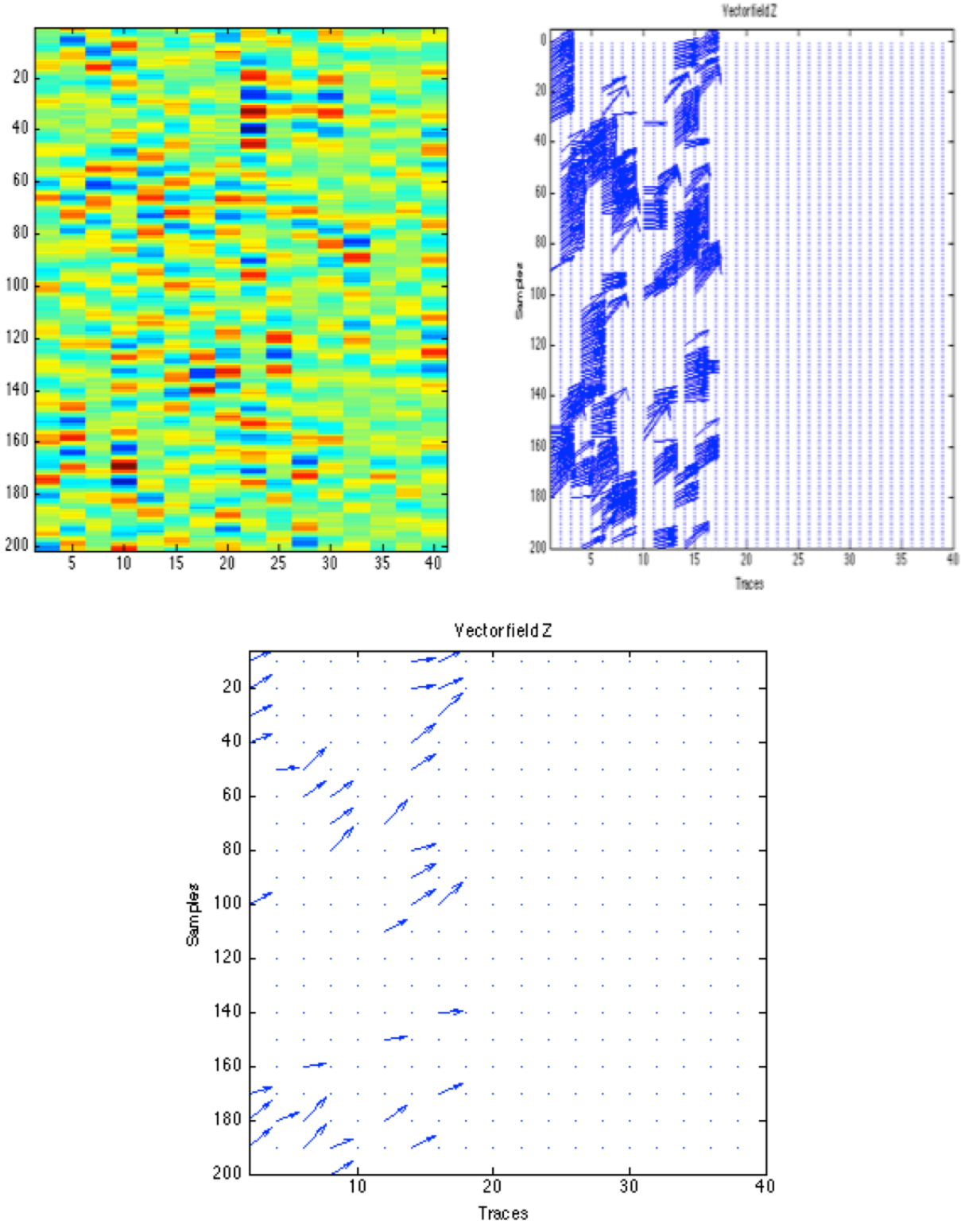

Figure 55: The Z-vector field (upper) and the sub-sampled Z- vector field (lower). The arrows represent the directions of SI. The dots represent areas where it is not possible to recognize the direction of SI.

9. CONCLUSION

Seismic exploration is one of the most significant techniques for discovering oil and gas reservoirs. Noise experienced during marine acquisitions is a common problem in the seismic industry since it reduces the data quality. Moreover, the process of noise removal is too costly and it takes a lot time.

One of the typical noises that occur during acquisition is seismic interference (SI). SI is caused by multiple seismic vessels operating in the same area. To prevent SI in the data gathers, a time-sharing procedure can carried out by the operating vessels. However, time-sharing results in wastage of time and it makes acquisition more costly.

A set of 2D marine multicomponent data (P, V_y, V_z) were investigated in this study, with the purpose of detecting and removing seismic interference noise. Parameters such as moveout and arrival time of the SI are beneficial to be identified in order to construct a noise model in the τ-p domain.

By sorting the (τ-p)-transformed seismic data to common-p we obtain a random appearance of SI and the noise can then be removed using random noise attenuation methods. This strategy has been proven to be efficient in this thesis work.

Characterization of seismic interference noise using V_z and V_y is not recommended because the particle motion sensor is sensitive to cable vibration. Therefore, the use of V_z and V_y component data for seismic interference noise removal is more difficult than using only conventional P-data.

Seismic interference noise from the P-data can be isolated using the τ-p to common-p method. It gives us a noise model that we subtract from the original shot by an adaptive subtraction. The SI-filtered shot gather can then be sorted into the CMP domain and stacked after NMO correction. Finally, the data can be imaged through post stack migration.

Stacking and post stack migration of the original shot gathers with SI noise show that fairly much the same results are obtained as in case of using pre-stack data after SI removal. This implies that migration is a strong denoising tool and that it can be used directly to remove

seismic interference noise from the original shot gather.

However, if we are interested in carrying out pre-stack studies like AVO (amplitude versus offset), it is important to have a technique available for filtering/removal of SI noise.

In the future, the multi-component streamer approach is likely to be improved due to new designs. Thus, a more comprehensive approach to characterize and removal of SI noise can then be foreseen if high-quality vectorized recordings are available.

BIBLIOGRAPHY

Gabrielsen, R. H. (2010), The structure and hydrocarbon traps of sedimentary basins. In: Bjørlykke, K. (Eds.), Petroleum geoscience: from sedimentary environments to rock physics. Springer, Heidelberg, Germany.

Caselitz, B., (2012). Attenuation Seismic Interference Noise Using a Dual Sensor Streamer.

Elboth, T. and D. Hermansen (2009). Attenuation of noise in marine seismic data. SEG Technical Program Expanded Abstracts: 3312-3316.

Fletcher, R., (2013). The formation of a failed continental breakup basin: The Cenozoic development of the Faroe-Shetland Basin. EAGE 25(5): 532-553.

Gelius, L. J. and T. A. Johansen (2010). Petroleum Geophysic. Bergen, UniGEO AS.

Geophysics, E. (1999). Basic Definations. From http://www.xsgeo.com/course/basic.htm.

Gulunay, N. (2008). Two different algorithms for seismic interference noise attenuation. The Leading Edge 27(2):1-6.

Jansen, S. (2013). Two marine seismic interference attenuation methods. Based on automatic detection of seismic interference, Master thesis, University of Oslo, Norway.

Jiuying, G., et al. High-amplitude Noise Attenuation. From http://www.cgg.com/technicalDocuments/0140.pdf.

Keary, P. B. M. H. I. (2002). An introduction to geophysical exploration. Oxford, Blackwell Science.

Maroof, S. and C. Gravely (1984). Aliasing and τ-p. SEG Technical Program Expanded Abstract: 623-625.

Moldoveanu, N., et al. (2007). Over/under towed-streamer acquisition: A method to extend seismic bandwidth to both higher and lower frequencies. From http://www.slb.com/~/media/Files/westerngeco/resources/articles/2007/jan07_tle_overunder.pdf.

O´Brien, P. E. (2002). IMPACTS OF MARINE ACOUSTIC TECHNOLOGY ON THE ANTRACTIC ENVIRONMENT. From http://www.bape.gouv.qc.ca/sections/mandats/sismiques/documents/DD2.pdf.

Pihl, R. (2007). Færøyene-natur. Retrieved 15.01, 2014, from http://snl.no/F%C3%A6r%C3%B8yene/natur.

Posthumus B. J. (1993). DEGHOSTING USING A TWIN STREAMER CONFIGURETION. Geophysical Prospecting, 41, 267-286.

Presterud, I. V. (2009). Time frequency de-noising of seismic data, Master thesis, University of Oslo, Norway.

Slubmberger (2013). Oilfield glossary. From http://www.glossary.oilfield.slb.com/en/Terms/n/noise.aspx.

Shepherd, R. (2002). Geology Map of Europe. Retrieved 19.01, 2014, from http://www.discoveringfossils.co.uk/europe_geology.htm.

Teigen, Ø. Et al. (2012). Characterization of noise modes in multicomponent data (4c) towed streamers. From http://www.slb.com/~/media/Files/technical_papers/eage/eage2012z013.pdf.

Yilmaz, Ö. (2001). SEISMIC DATA ANALYSIS. USA, Society of Exploration Geophysicists.

APPENDIX: Complete processing flowchart

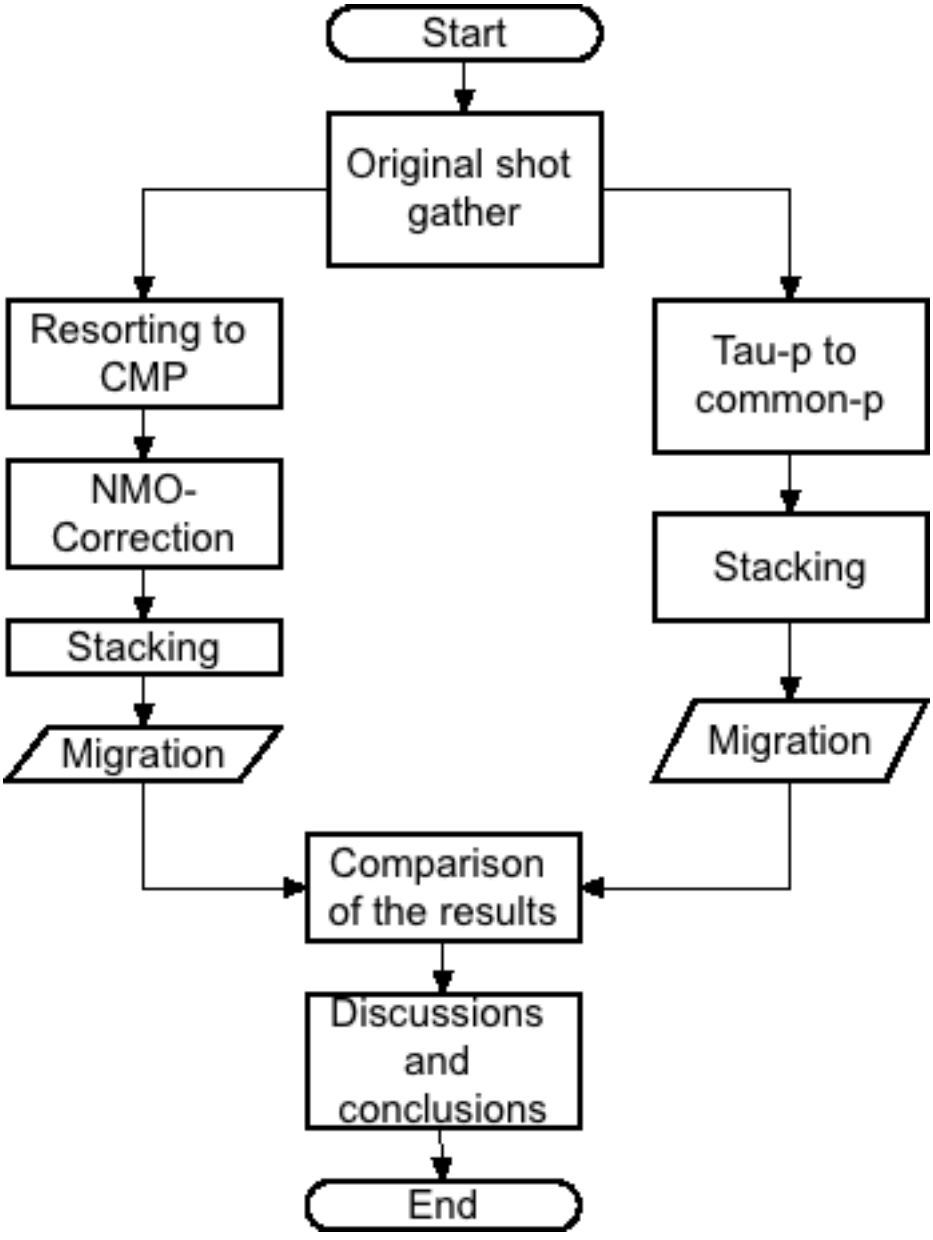

Figure A.1: Complete processing flowchart.